POLITECNICO DI TORINO

Master's Degree in Electrical engineering

Master's Degree Thesis

Dedicated Modeling of Electric Motors for Hybrid Electric Powertrains

Supervisors

Prof. Alberto TENCONI

Prof. Silvio VASCHETTO

Candidate

Giuseppe LIBRALE

07/2023

Abstract

The electrification of transport, particularly in the automotive industry, refers to the transition from traditional internal combustion engine (ICE) vehicles to electric vehicles (EVs) powered by electricity. This shift is driven by the need to reduce greenhouse gas emissions, mitigate climate change, and address environmental concerns associated with fossil fuel consumption. There are several advantages to using electric vehicles compared to traditional ICE vehicles. First and foremost, EVs produce zero tailpipe emissions, reducing air pollution and improving air quality. The electrification of automotive transport presents opportunities for increased energy efficiency. Electric vehicles are powered by one or more electric motors, which are fueled by rechargeable batteries. Electric motors are generally more efficient than internal combustion engines, converting a higher percentage of stored energy into motion.

This thesis work concerns the electromagnetic study of an e-motor, in detail an IPM-SynRM from the Toyota Prius. The purpose of this study is to obtain a model of the machine that describes it in energetic way. This model is represented by the efficiency map of the machine through which a thermal study of the system can be performed. It is important to specify the thermal study is not in the frame of this work.

The used strategy combines FEM simulations with machine's analytical model in order to obtain accurate data with the aim to save computation time since to simulate the motor in all possible conditions, thousands of analyses have to be done.

Table of Contents

List of Tables

List of Figures

Introduction

Environmental problems and the regulations created to combat them have led to a general hybridization of the transportation system in order to minimize emissions. However, it is important to understand if this transition is possible and how it can be made. In this direction, as with internal combustion engine vehicles, the virtualization of electric ones is essential. The opportunity of create a virtual versions of electrical components makes possible the simulation of systems based on this technology.
An electric vehicles power-train consists of some fundamental parts: battery, vehicle, transmission, e-motor, power electronic components and cooling system. At this time it is feasible to evaluate the behaviour of each single previously mentioned parts and simulate the performance of a system that includes them all. There are different approaches to model the eDrive components, each has its strengths and disadvantages. These techniques can be resumed as follow:

- **Constant efficiency**: it is assumed that power converter and e-motor work at constant efficiency. It is affordable and simple for energetic assessment, but it leads low accurate results if the power-train is not operated at fixed working point.
- **Efficiency map model**: e-motor and power converter efficiencies are mapped in some working point in the operative torque-speed plane and voltage-current one.Its accuracy depends on the maps discretisation and on the operative conditions to which the maps refer.
- **Equivalent circuit models**: the e-motor behaviour is described by a single phase equivalent circuit, in steady state conditions. The strong point is the low computation time.
- **Analytical models**: eDrive is modelled through a set of electric, magnetic and mechanical derivative equations. The computation time depends on the required results accuracy.
- **Computer-aided engineering models**:this approach models the power-train using finite element models in order to obtain very detailed data. It

requires a complete knowledge of the eDrive components and high expertise on the model definition. It is very time consuming.

- **Co-simulation platforms**: it integrates the advantages of different software into a single simulation. Its accuracy and computational time are high.

The purpose of this thesis work is to conclude a first stage that make possible to carry out an e-drive thermal study. This first step includes an electromagnetic analysis of the e-motor in which some efficiency map in different conditions (maximum voltages and temperatures) can be extracted.

Structure of the thesis

This thesis work is organized in this way:

- In **Chapter 1** the different types of e-motor used for traction in the automotive sector are described, indicating the various strengths and weaknesses for which one type of machine provides better performance than the other. At the end of this chapter, all data of the studied motor, 2010 Toyota Prius motor, are illustrated.
- In **Chapter 2** the strategy by which the purpose of this work is reached.
- In **Chapter 3**, the correctness of the model created on the fem is analysed by means of preliminary analyses concerning the waveforms of the no-load voltages of the machine and the torque trend for certain currents (nominal and overload conditions). The results of this chapter are compared with those obtained in some articles in the references. If they correspond, the model is considered correct.
- **Chapter 4** includes all the simulations carried out in the FEM environment to extract all the parameters and inputs that will then be used to create the analytical model of the machine. This chapter is separated from the previous one even though it always deals with simulations in the FEM environment because the tests illustrated in Chapter 3 are only preliminary tests, which are not included in the method used in this thesis work.
- Once all model parameters and inputs have been obtained in the previous chapters, the algebraic model is analysed in **Chapter 5** with all final results, as the efficiency maps.

Chapter 1

State of the art of hybrid and electric power-train

This chapter offers a quick overview of the state of the art of the main electrical components used in HEV and EV traction. Since the scope of this project is a first stage to make possible a thermal study of the power-train, battery pack will not be examined because it is cooled by a separate cooling system.
As will be seen below, the analysis of the inverter will also be omitted as it consists of a simple analytical analysis, so only an in-depth analysis of the motor studied in this project thesis will be made in order to make the modeling easier.
At the end of this chapter a description of the studied motor will be made.

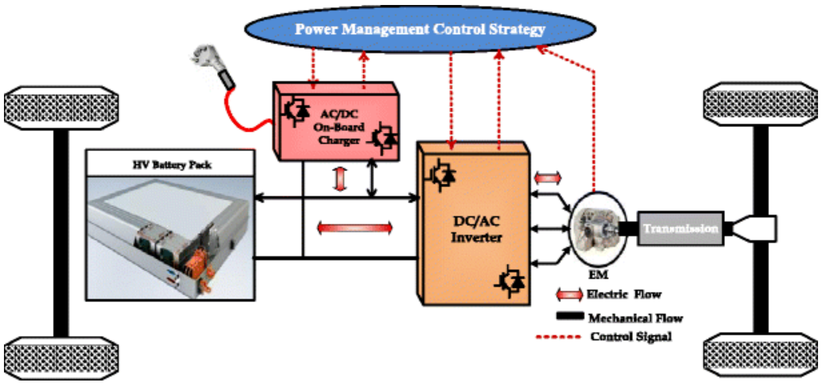

Figure 1.1: Example of electric powertrain.[1]

1.1 Electric Motors

The automotive industry has witnessed significant advancements in recent years, with a strong focus on sustainable and environmentally friendly technologies. One of the key drivers behind this transformation is the emergence and rapid development of electric motors, also known as e-motors, for automotive applications. E-motors have revolutionized the way we think about transportation, offering numerous benefits in terms of efficiency, performance, and reduced environmental impact.

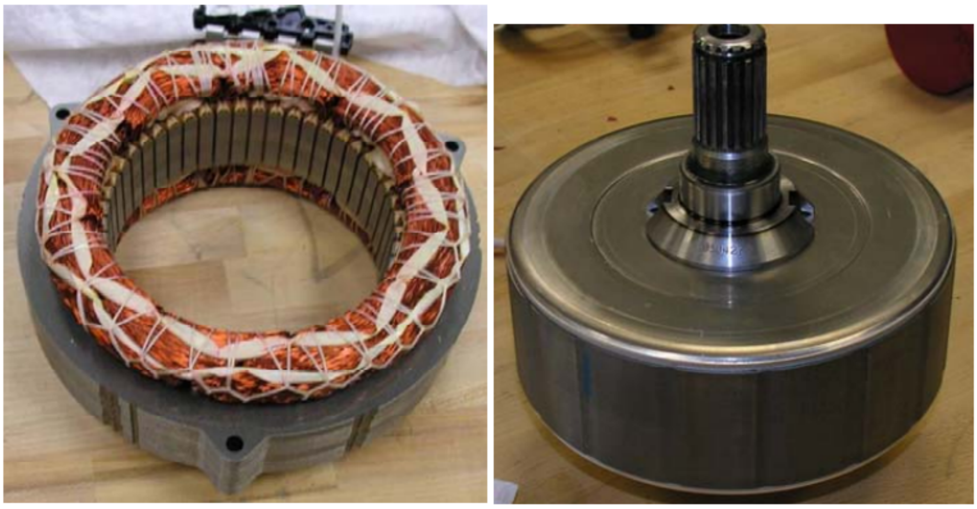

Figure 1.2: 2010 Toyota Prius e-motor.[2]

E-motors are the heart of electric vehicles (EVs), powering them with electricity instead of relying on traditional internal combustion engines. This shift towards electrification has gained momentum as governments, automakers, and consumers alike recognize the pressing need to transition away from fossil fuels and reduce greenhouse gas emissions. E-motors play a pivotal role in enabling this transition and reshaping the automotive landscape. The primary advantage of e-motors lies in their remarkable efficiency compared to internal combustion engines. Traditional engines convert only a fraction of the energy derived from burning fuel into mechanical power, while the rest is lost as heat. In contrast, e-motors are highly efficient, with energy conversion rates exceeding 90%. This efficiency translates into improved range and reduced energy consumption, making electric vehicles an attractive and viable alternative to conventional gasoline-powered cars. E-motors also offer exceptional performance characteristics. Unlike internal combustion engines that require time to reach peak torque, e-motors provide instant torque from the moment they are activated. This instant acceleration delivers a thrilling driving experience, with EVs often outperforming their gas-powered counterparts in terms of acceleration and responsiveness. Additionally, e-motors provide a smooth and quiet operation, enhancing the overall comfort and refinement of electric vehicles. Another significant advantage of e-motors is their reduced maintenance requirements. Unlike internal combustion engines, e-motors have fewer moving parts, eliminating the need for components such as pistons, valves, and timing belts. This simplification results in lower maintenance costs and increased reliability. Electric vehicles equipped with e-motors require less frequent servicing, as there is no need for oil changes or complex engine tune-ups. Furthermore, e-motors contribute to a cleaner and greener environment. By eliminating tailpipe emissions, electric vehicles powered by e-motors help reduce air pollution and decrease our carbon footprint. They offer a sustainable transportation solution, especially when coupled with renewable energy sources for charging, such as solar or wind power. This combination of e-motors and clean energy fosters a more sustainable and eco-friendly transportation ecosystem. The advancements in e-motor technology have also led to the development of various types of electric motors, each suited for specific applications. Permanent magnet synchronous motors (PMSM) and induction motors are two commonly used types. PMSM motors offer high power density and efficiency, making them ideal for electric vehicles. Induction motors, on the other hand, are known for their robustness and cost-effectiveness, often found in hybrid vehicles. Each type of e-motor will be described below.

1.2 Induction Motor

An induction motor is a type of alternating current (AC) electric motor widely used in various applications, from industrial machinery to household appliances. The induction motor is also known as an asynchronous motor because the speed of the rotor always lags behind the speed of the rotating magnetic field produced by the stator. This speed difference, called slip, is necessary to induce current in the rotor and generate the torque required for the motor to operate. The asynchronous nature of the motor makes it reliable, simple, and cost-effective. The rotor of an induction motor commonly consists of a cylindrical core made of laminated iron and conductive bars arranged in a parallel manner across its length. These bars are shorted at the ends by conducting rings, forming a structure that resembles a squirrel cage. Hence, the rotor is often referred to as a "squirrel cage rotor." The conductive bars in the rotor cage allow the induced currents to flow, interacting with the magnetic field produced by the stator and generating a torque that drives the rotor in the same direction as the rotating magnetic field.

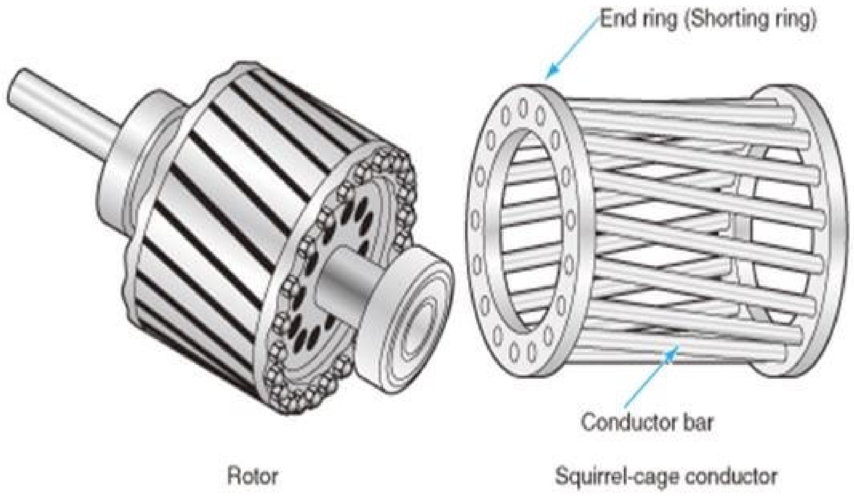

Figure 1.3: Example of squirrel cage of induction motor.

This motor was widely used before the improving of the inverter, due to the start-up semplicity. In particular, in the automotive world now it is used as an addition traction supply, as in Tesla, because of the ability to break away from traction: it provides torque in acceleration to increase the performances, but at high speed it is switched off and not having permanent magnets, it does not produce losses when the rotor turns. The reason why this type of motor is no longer widely used for electric traction is because of the need for so much torque and high efficiency. In fact, induction motor is more overloadable but it has a lower torque density than permanent magnet motors. In addition, the presence of currents in the rotor bars means higher losses and lower efficiency. For these reasons, this type of engine will not be considered in this thesis work.

1.2.1 Control capability curves of IM

Assuming a current control in dq coordinates, it is convenient to understand the main characteristic curves of this type of machine in order to discuss advantages and disadvantages for automotive application.

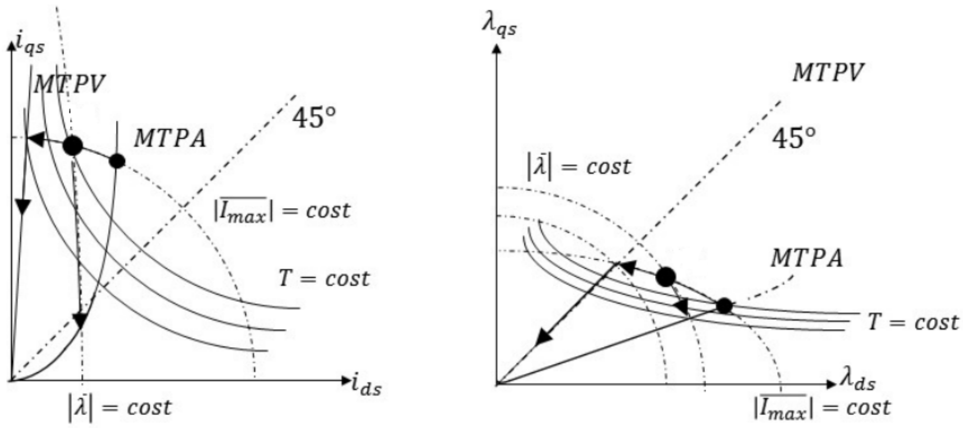

Figure 1.4: Control capability curves of IM.[3]

Fig.1.4 shows the MTPA and MTPV profiles of the Induction Motor on currents and fluxes plane in dq coordinates. As will be described later, Max Torque Per Ampere profile (MTPA) is the place of working point in which it is possible to obtain the maximum torque to the shaft for each current value. It is the same concept for MTPV, but related to the voltage. As it can be seen, for IM all these working points are placed in first quadrant. This means that the motor needs higher current, because a part of the stator current is used to magnetize the machine. This higher value causes higher losses, so lower efficiency. In addition, rotating magnetic field induces currents to the rotor cage, that causes additional losses. As an advantage, however, this feature allows the machine to be perfectly decoupled from the drive as mentioned above.

1.2.2 Dynamic curves of IM

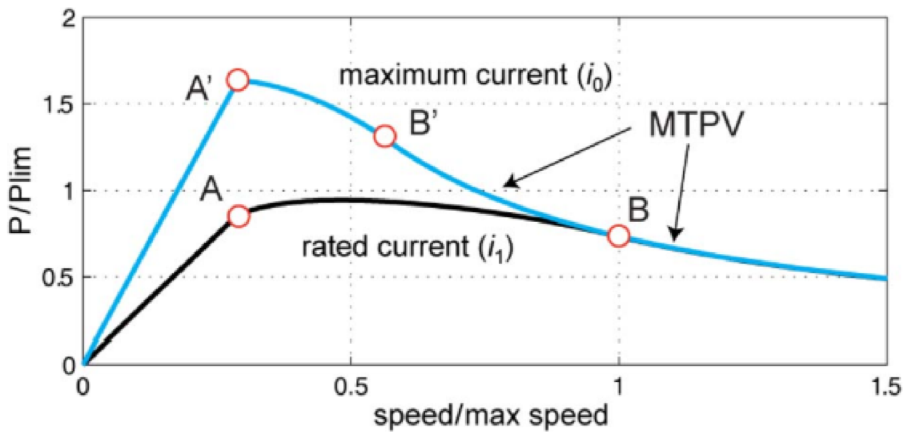

Figure 1.5: Dynamic curves of IM.[3]

Fig.1.5 shows a common trend of the power in function of speed for an induction motor. This type of machine is over-loadable in both current and temperature because not having magnets, demagnetization problems do not exist.
On the other hand, at high speed power trend is negative, so the constant power region is small. This means that this motor can not reach high speed providing the maximum power, so the insertion of a gearbox may be necessary as the automotive application requires very high speeds, but gearbox introduces additional losses.

1.3 Permanent Magnets motors

A permanent magnet motor, also known as a permanent magnet synchronous motor (PMSM), is a type of electric motor widely used in automotive applications. It utilizes permanent magnets embedded in the rotor to create a magnetic field, which interacts with the rotating magnetic field produced by the stator to generate torque. In the context of automotive systems, permanent magnet motors have gained significant attention and adoption due to their high efficiency, compact size, and excellent power-to-weight ratio. These motors are commonly employed in electric and hybrid vehicles for propulsion and various auxiliary functions. The rotor of a permanent magnet motor, as shown in fig.1.6 consists of a cylindrical core with permanent magnets mounted on its surface, often made of materials such as neodymium or ferrite. These magnets create a fixed magnetic field that remains constant as the motor operates, eliminating the need for additional field windings or excitation circuits. This design simplifies the motor construction and improves its efficiency.

Figure 1.6: Example of rotor with permanent magnets.

The stator, which surrounds the rotor, comprises a series of windings that produce a rotating magnetic field when energized with alternating current (AC). The interaction between the stator's rotating magnetic field and the fixed magnetic field of the rotor generates torque, causing the rotor to rotate. One of the significant advantages of permanent magnet motors in automotive applications is their high power density. They offer a high torque output relative to their size and weight, enabling them to deliver strong acceleration and improve overall vehicle performance. Additionally, permanent magnet motors have excellent controllability, allowing precise control over motor speed and torque, which is crucial for achieving efficient energy conversion and optimizing vehicle efficiency. Furthermore, permanent magnet motors exhibit high efficiency across a wide range of operating speeds and loads. This efficiency is beneficial for electric and hybrid vehicles, as it helps maximize the vehicle's range and battery life. Permanent magnet motors have emerged as a key technology in the automotive industry, providing efficient and reliable solutions for various vehicle applications, including electric propulsion, power steering, regenerative braking, and other auxiliary systems. Their compact

size, high power density, and excellent performance characteristics make them well-suited for the demanding requirements of modern automotive applications.
As studies on permanent magnet electric motors progressed, several types of e-motors emerged. These motor are divided into two main families: Surface Permanent Magnets motors (SPM motors) and Interior Permanent Magnets motors (IPM motors). As shown in fig.1.7 they differ only in the type of rotor: for the SPM (left side in figure) magnets are placed on the rotor surface whereas for the IPM ones (right side) they are allocated into the rotor.

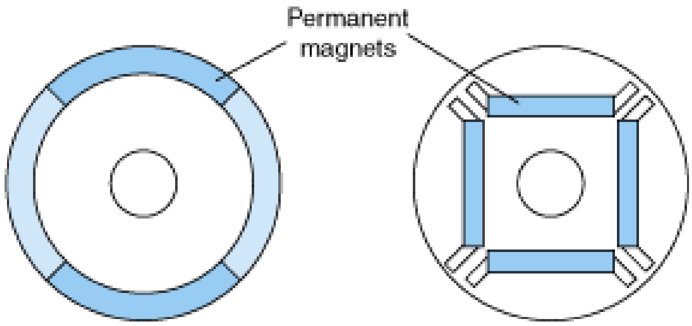

Figure 1.7: Left side: Surface Permanent Magnet rotor;
Right side: Interior Permanent Magnet rotor

1.3.1 Surface Permanent Magnets Motors

In an SPM motor, the rotor consists of a series of permanent magnets that are mounted on the surface, typically in a radial or axial arrangement. These magnets generate a magnetic field that interacts with the stator winding's magnetic field, causing the rotor to rotate. This type of machine shares some characteristics and advantages with IPM one, because are both permanent magnet motors. Some differences can be explained studying behaviour in terms of performances: control curves and dynamic curves.

1.3.2 Control capability curves of SPM motor

As seen for IM, control capability curves describe how the motor works.

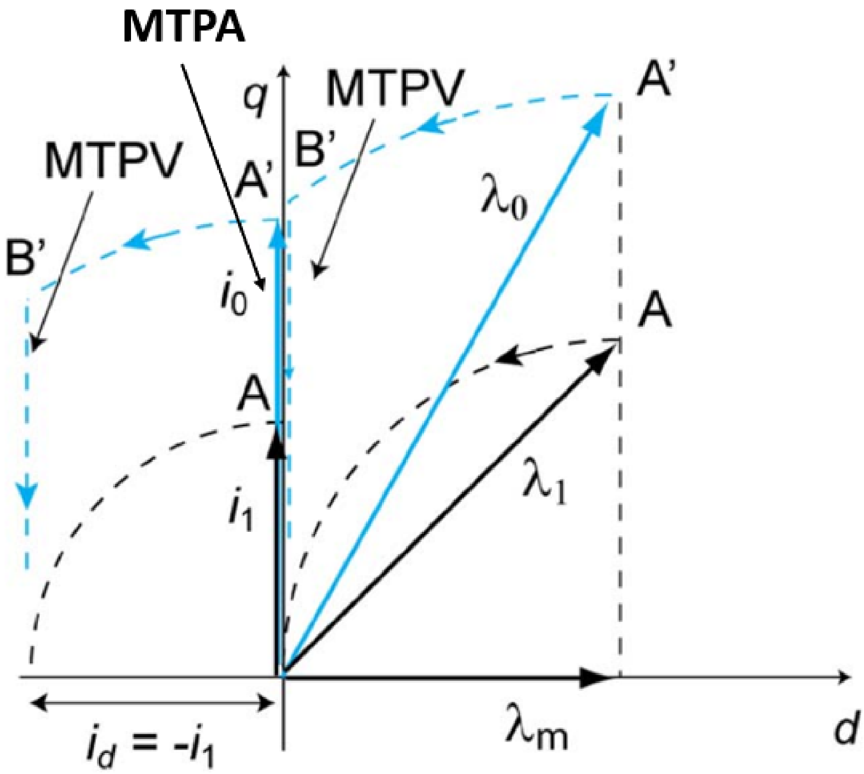

Figure 1.8: Control capability curves of SPM motor.[3]

Fig.1.8 shows the SPM control capability curves in dq plane. Two different conditions are described: standard conditions (black vectors) and overload ones (blue vectors).
Having magnets on the rotor, machine doesn't need to be magnetized by stator current, so all the current applied to the stator winding contribute to create torque. MTPA profile is placed on q-axis, this make easier the control of the motor, this is the main advantage of this type of PM motor. Once the base speed has been exceeded flux weakening is needed, so a term of current that demagnetized the motor is generated. This aspect implies a constant power range wider than IM one, as it can be seen in the next paragraph.

1.3.3 Dynamic curves of SPM motor.

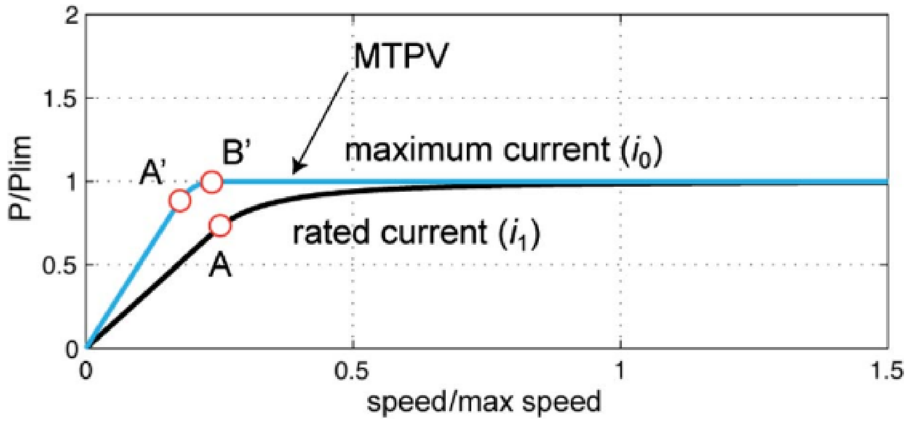

Figure 1.9: SPM dynamic curves.[3]

As said before in this paragraph dynamic curves of SPM are shown, in detail in fig.1.9. In contrast to the induction motor, this type of machine is not overloadable due to the presence of the magnets: if the current is too high, or the temperature too, they can be demagnetized. On the other hand, this motor has a wide range in which the power is constant and equal to the maximum value.

1.3.4 Internal Permanent Magnet motor

An internal permanent magnet (IPM) motor is a type of electric motor that utilizes permanent magnets embedded within the rotor structure. The design of IPM motors combines the advantages of both permanent magnet motors and induction motors, resulting in improved efficiency, power density, and control performance.

Here are some key features and characteristics of internal permanent magnet motors, some of them are in common with SPM:

- Rotor Configuration: In an IPM motor, the rotor consists of a cylindrical core made of magnetic material, such as iron or steel, with permanent magnets embedded in it. The permanent magnets are usually made of rare-earth materials like neodymium-iron-boron (NdFeB) or samarium cobalt (SmCo).
- Magnetic Field Interaction: as permanent magnet motors, magnets in the rotor create a magnetic field that interacts with the stator's rotating magnetic field. This interaction generates torque, enabling the motor to produce mechanical work.
- High Torque Density: IPM motors have a high torque density due to the presence of strong permanent magnets in the rotor. This means they can deliver higher torque output for a given motor size, making them suitable for applications where space and weight constraints exist. Actually, the position of the magnets, embedded in the rotor structure, creates an anisotropy behaviour that creates an additional torque in respect to the SPM, the reluctance one.
- Improved Efficiency: in general, for all Permanent magnet motors, the use of permanent magnets contributes to their higher efficiency compared to induction motors. The permanent magnets help reduce energy losses associated with rotor resistance, resulting in improved overall motor efficiency.
- Wide Speed Range: IPM motors are capable of operating over a wide speed range, offering good performance at both low and high speeds. As before, this will be demonstrated by dynamic curves. This versatility makes them suitable for various applications, including electric vehicles, robotics, industrial machinery, and HVAC systems.
- Precise Control: IPM motors provide excellent control performance due to the presence of permanent magnets, which enhances the motor's response and accuracy. This makes them well-suited for applications requiring precise speed control, such as servo systems.
- Regenerative Braking: IPM motors are capable of regenerative braking, meaning they can recover and convert kinetic energy back into electrical energy

during deceleration or braking. This feature improves energy efficiency and reduces wear on mechanical braking systems.

- Cooling Considerations: Since the permanent magnets in IPM motors can be sensitive to high temperatures, proper cooling mechanisms are crucial to maintain their performance and longevity. Techniques such as liquid cooling or incorporating cooling channels in the motor design help dissipate heat effectively.

Magnets embedded in the rotor structure allow for different possibilities of positioning the magnets. Fig.1.10 shows some different type of rotors with magnets embedded in the structure.

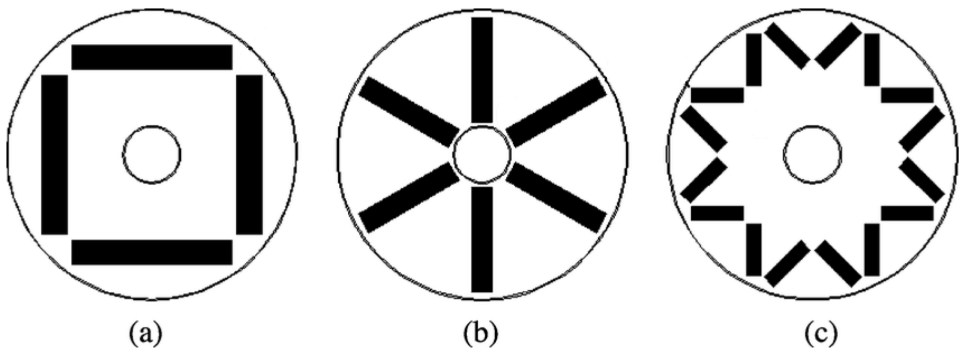

Figure 1.10: Different rotor typologies.[4]

Each type of rotor has its strengths, in detail the rotor most commonly used in the automotive industry is on the same line as the one in the fig.1.10.c. It has a V-shaped orientation of the magnets that causes an anisotropic behaviour of the rotor that combines the advantages of a permanent magnet motor with a synchronous reluctance motor ones, creating an Internal Permanent Magnet Synchronous Reluctance motor, also called "IPM-SynRM". In these motors torque is composed by two terms: magnets one, and reluctance one. In addition, the behaviour at high speed is improved: constant power speed range is the widest.

1.3.5 Control capability curves of IPM motor.

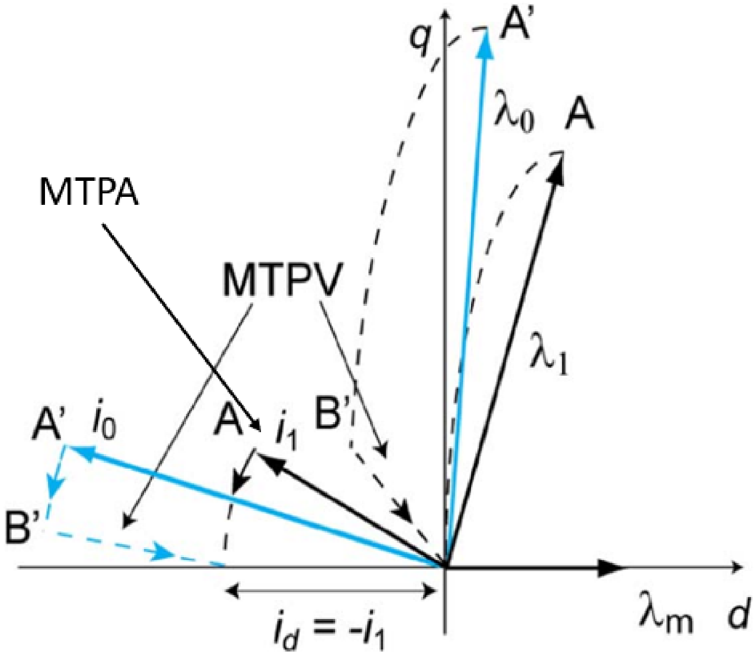

Figure 1.11: Control capability curves of IPM motor.[3]

As the SPM motor, in fig.1.11 control capability curves are shown and, as for the SPM machine is magnetized by magnets, so no current term for magnetizing the motor is needed. However, in this case, the MTPA profile is not placed on the q axis, but in the second quadrant due to the anisotropic behaviour. The angle of this curve can change depending on the typology of the rotor. The flux weakening is similar to the SPM motor.

1.3.6 Dynamic curves of IPM motor.

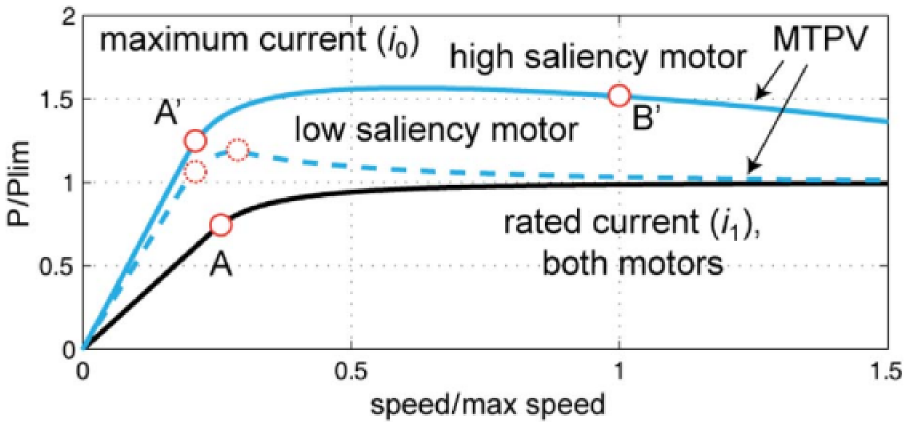

Figure 1.12: Dynamic curves of IPM motor.[3]

Fig.1.12 shows the dynamic curves of the IPM motor. All the considerations made for the dynamic curves of the SPM also apply to the IPM, but in this case it can be seen that, in overload conditions, by increasing the rotor saliency, the curve tends to rise and reach a higher maximum power than that of the SPM. This leads to a wider constant power region, making this type of motor one of the best for automotive applications.

1.4 2010 Toyota Prius motor

The motor of the 2010 Toyota Prius is an internal permanent magnet motor with a V-shaped orientation of magnets, one of the most widely used, as explained before, in the automotive world. In table 1.1 are shown main features of the machine.

Figure 1.13: 2010 Toyota Prius rotor.[2]

Toyota Prius 2010		
P_{max}	60	kW
T_{max}	207	Nm
ω_{max}	13500	rpm
V_{bus}	650	V
I_N	120	A
Poles	8	

Table 1.1: Main parameters Toyota Prius 2010 motor.

When creating the magnetic model, what is important to know are the geometric dimensions, the type of winding and the characteristic of the magnets. These aspects will be described below.

1.4.1 Geometric dimensions

Regarding motor geometry, the data is summarised in the tables below. Note that some of the more detailed data such as the dimensions of the different air gaps in the rotor are quite approximate as they are hard to find. In any case these approximations will have negligible effects for the purposes of the study.[2] [5] [6] [7] [8]

Lamination dimensions		
Stator outer diameter	264	mm
Stator inner diameter	161.9	mm
Stack length	50.8	mm
Rotor outer diameter	160.4	mm
Rotor inner diameter	51	mm
Air gap	0.73	mm
Lamination thickness	0.305	mm

Table 1.2: Dimensions of lamination parts.

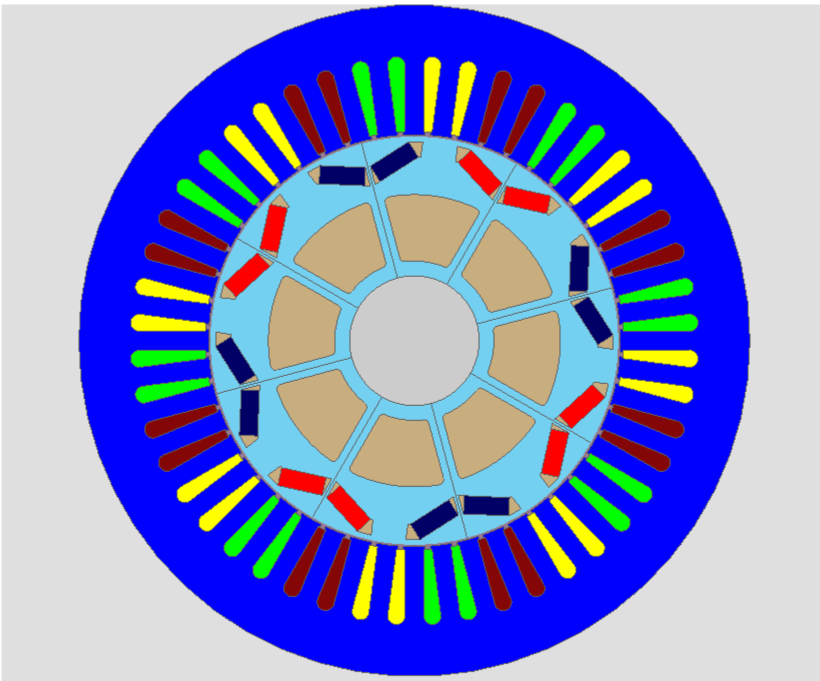

Figure 1.14: 2010 Toyota Prius Motor Altair Flux model.

Other dimensions		
Slot opening	1.88	mm
Slot depth	30.9	mm
Rotor bridge thickness	1.99	mm
Magnet angle	145	degree
Rotor air gap bridge width	5.8	mm

Table 1.3: Dimensions of stator and rotor parts.

1.4.2 Winding

As far as winding is concerned, it is a simple three-phase sinusoidal distribution one. Each phase of the 2010 Prius motor stator windings is composed of 8 coils in series, each coil is made of 11 turns, each turn consists of 12 – 20 AWG wires (American Wire Gauge). Winding characteristics are summarised in the table 1.4.

Windings		
Number of stator slots	48	
Stator turns per coil	11	
Parallel circuits per phase	0	
Coils in series per phase	8	
Number of wires in parallel	12	
Wire size	20	AWG
Phase resistance at 21°C	0.077	Ω
Total mass of stator copper	4.93	kg

Table 1.4: Windings characteristics

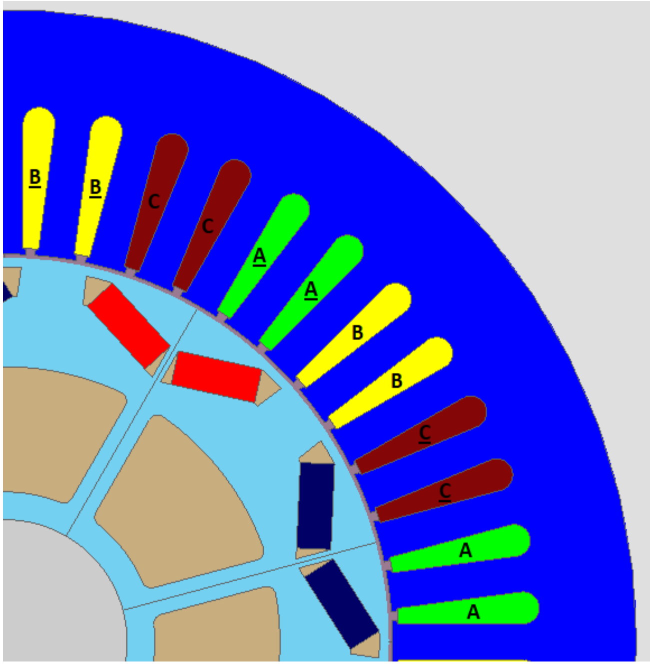

Figure 1.15: Winding scheme.

1.4.3 Magnets

Magnets used for the motor are of the rare-earth type. In [2], different hysteresis tests have been done. These kind of tests provide information regarding the remanent flux density and coercivity of a magnet and they are often conducted over a wide range of temperatures. In table 1.5 magnet dimensions are shown. Note that there is a value of B_r, in (in test back-emf) it will be explained why that value was chosen

Magnet dimensions		
Depth	49.3	mm
Width	17.88	mm
Height	7.16	mm
Volume	6.31	cm^2
Mass	48	g
Total mass of magnet	0.768	kg
B_r **at 120°C**	1.18	T

Table 1.5: Magnet dimensions

Fig.1.16 shows how the characteristics of the magnets change with the temperature. As said before, one of the main problems of the Permanent Magnet Motor is the temperature, in fact in this figure it is clear how temperature tends to demagnetize magnets, making the motor less performing.

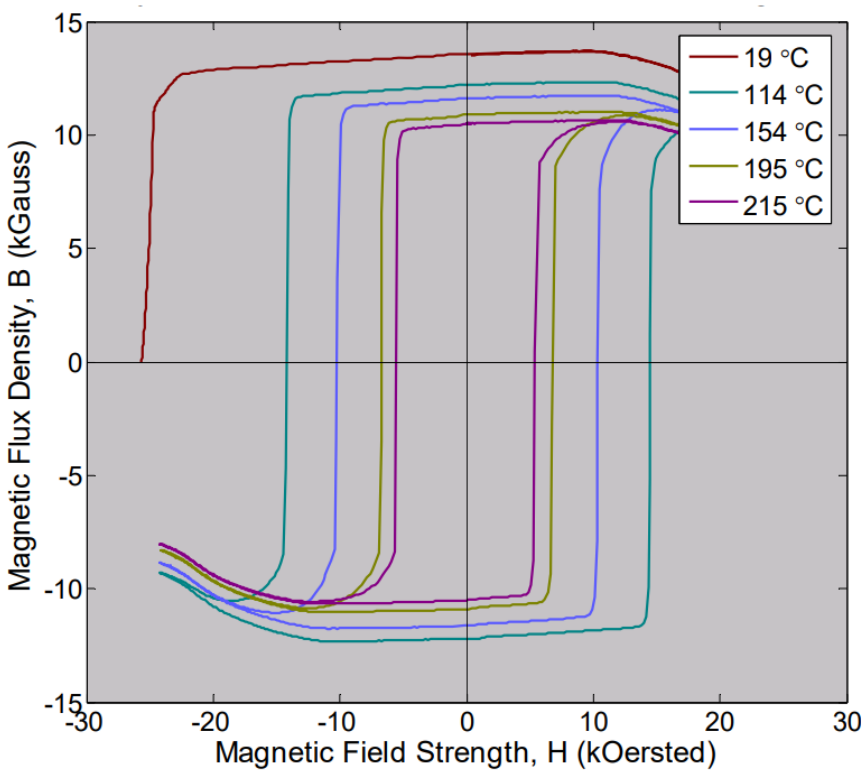

Figure 1.16: Intrinsic hysteresis graphs for 2010 Prius motor magnet at various temperatures. [2]

Chapter 2

Evaluation strategy analysis

In this chapter the approach used to model and simulate the hybrid power-train will be described. Following mapping algorithm is developed for eDrives that consist of an Internal Permanent Magnet Synchronous Reluctance Motor (IPM SynRM) supplied by a Voltage Source Inverter (VSI). The purpose of the model is to obtain a set of efficiency maps for the electric machine and the power converter in the torque-speed plane and for different levels of supply voltage and machine working temperatures.

Each model approach needs of inputs, in this type of analysis the inputs are: the magnetic model of the machine, iron losses and the stator resistance. It is important to specify what makes competitive this approach: the limited computation time required to obtain the complete set of efficiency map compared with a different methods (FEM or experimental). Obviously, computation time and accuracy depend of the number of working point in which input parameters are available, increasing this number accuracy grows up, but the study will be longer.

From a thermal/energetic point of view, for the conversion stage (the inverter) there aren't any particular problems because its losses are calculated by some formulas having only the current stress. So the inverter study will not examined in this work.

Input parameters are provided as different maps, that depend on frequency, machine temperatures and torque. Following sections explain how to get these maps.

2.1 IPM electromagnetic model

Before describing the electromagnetic model, it is important to show hypothesis in which this model is valid:

- Magnetic linearity;
- Magnetic induction is assumed sinusoidal: only the first harmonic is considered;
- To simplify the questions, one pole pairs is considered;
- The machine is a synchronous anisotropy one with permanent magnets embedded in the rotor structure.

To explain the algebraic model, it is necessary to start from the main equations describing a three-phase machine: electrical and magnetic equations, shown in

$$\overline{V}_{123} = R_s \overline{I}_{123} + \frac{d\overline{\lambda}_{123}}{dt} \tag{2.1}$$

$$\overline{\lambda}_{123} = L_{ls}\overline{I}_{123} + [L_{123}]\overline{I}_{123} + \overline{\lambda}_{PM} \tag{2.2}$$

where:

- V_{123} represents the stator voltage in the time phase domain;
- I_{123} stands for the stator current;
- λ_{123} stand for the magnetic flux concatenated with stator windings;
- L_{123} is stator inductance matrix;
- λ_{PM} is the flux produced by the PM;
- L_{ls} is the leakage stator inductance, which is constant for each phase.

Three-phase to dq axes transformation is required to make simpler the computation. Clarke matrix first and the rotation matrix later are the elements for this transformation. The angle represents the position of the rotor, so the PM flux is aligned with d-axis. Each elements are presented below.

$$[\mathrm{C}] = \begin{bmatrix} 2/3 & -1/3 & -1/3 \\ 0 & 1/\sqrt{3} & -1/\sqrt{3} \\ 1 & 1 & 1 \end{bmatrix} \qquad [\mathrm{R}(\theta)] = \begin{bmatrix} cos(\theta) & sin(\theta) \\ -sin(\theta) & cos(\theta) \end{bmatrix}$$

Now electrical and magnetic equations using in IPM modelling in dq axis can be written as:

$$\begin{cases} v_d = R_s i_d + L_d \frac{di_d}{dt} - p\omega_r \lambda_q \\ v_q = R_s i_q + L_q \frac{di_q}{dt} + p\omega_r \lambda_d \\ \lambda_d = L_d i_d + \Lambda_{PM} \\ \lambda_q = L_q i_q \end{cases}$$

For this type of analysis, steady state conditions are considered, so final equations are shown below:

$$\begin{cases} V_d = R_s I_d + L_d \frac{dI_d}{dt} - p\omega_r \Lambda_q \\ V_q = R_s I_q + L_q \frac{dI_q}{dt} + p\omega_r \Lambda_d \\ \Lambda_d = L_d I_d + \Lambda_{PM} \\ \Lambda_q = L_q I_q \end{cases}$$

These equations describe the equivalent circuit of the machine in dq axes, shown in fig.5.5

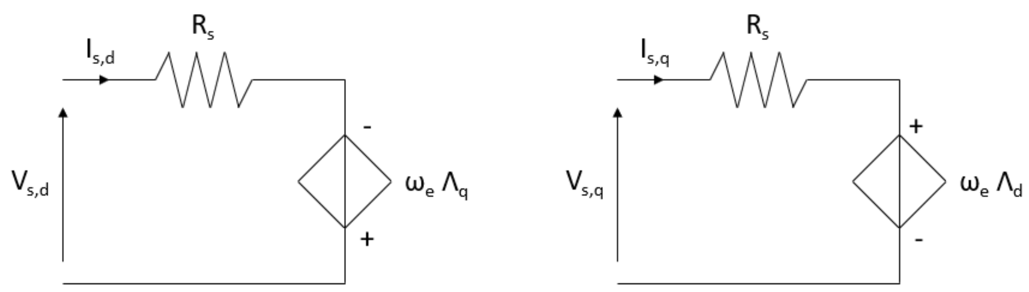

Figure 2.1: Equivalent circuit of IPM machine in dq axes.

As a thermal study, a parameter that represents iron losses has to be added. These type of losses depend on the voltage of the machine, so they can be described by a fictitious resistance in parallel with pilot generator $\omega_e\Lambda_d$ and $\omega_e\Lambda_q$, as illustrated in fig.2.2

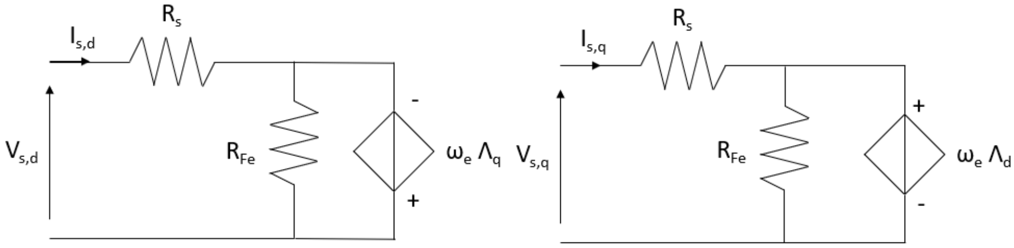

Figure 2.2: Equivalent circuit of IPM machine with iron losses.

A Thevenin simplification is performed because the magnetic maps take into account the equivalent currents, without losses terms. Final equivalent circuit is shown in fig.2.3

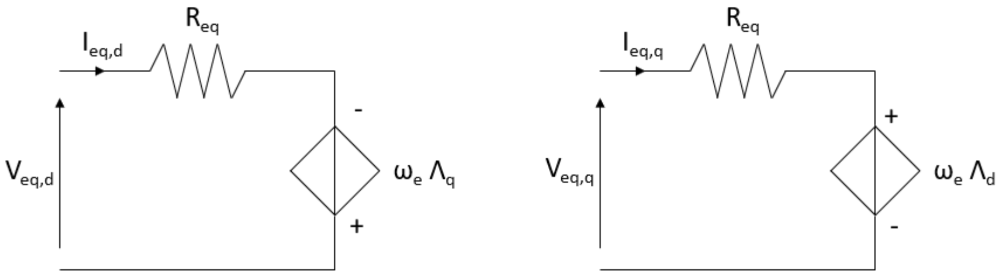

Figure 2.3: Equivalent Thevenin simplification.

By Thevenin simplification new parameters and new variables are presented:

$$R_{eq} = \frac{R_s R_{Fe}}{R_s + R_{Fe}} \qquad \overline{V}_{eq} = \overline{V}_s \frac{R_{Fe}}{R_s + R_{Fe}} \qquad \overline{I}_{eq} = \overline{I}_s - \overline{I}_{Fe} \tag{2.3}$$

Finally, it is possible to compute the iron losses equivalent current using the superposition principle, as below:

$$\overline{I}_{Fe} = \overline{V}_s \frac{1}{R_s + R_{Fe}} - \overline{I}_{eq} \frac{R_s R_{Fe}}{R_s + R_{Fe}} \tag{2.4}$$

At this point, after appropriate computations, electromagnetic torque equation is performed:

$$T_{em} = \frac{3}{2}p(\Lambda_d I_{eq,q} - \Lambda_q I_{eq,d}) \tag{2.5}$$

The useful torque at the shaft is:

$$T_m = T_{em} \pm T_{fv} \tag{2.6}$$

where T_{fv} is the friction and ventilation torques, which can be modeled as polynomial.

After describing the algebraic model of the machine, it is necessary to understand how all the parameters of the model are obtained. Table 2.1 shows how different parameteres are calculated.

Parameter Map	**Procedure**	**Dependence**
Stator resistance	Manufacturer data	Temperature and speed
Equivalent iron resistance	Simulations	Torque and speed
Magnetic maps	Simulations	PM Temperature
Mechanical losses	Measurements	Speed

Table 2.1: Procedure to compute parameters' map.

In this thesis work, mechanical losses and skin effect in conductors are not considered not having experimental results. Nevertheless, random mechanical losses could be taken into account for efficiency map to show the dependence. The procedure for extracting the flux maps of a machine and the fictitious resistance map representing the losses in the iron will be described in this chapter.

2.1.1 Flux maps extrapolation

As said above, magnetic maps will be extrapolated by FEM environment and depend on PM temperature, in fact, as shown in 1, the value of magnet's residual induction decrease when temperature rise up. So each value of temperature will provide a different magnetic map.
Procedure is very simple but is the longer part of this work too because of FEM simulations. Basically, once the machine model has been created in a fem environment, various tests will be carried out to assess the correctness of the model, such as air gap flux density and back-electromotive forces tests. If results are as expected position of dq axes will be compute as the angle between d axis and the first phase axis. The computation consists of taking into account a grid in dq axes, as shown in fig.2.4, providing the current vector, representing by each point, to the stator winding, so using inverse transformation described before. In each working point of the grid, rotor will be rotated for at least an electrical period. It is really important considering whole periods to avoid errors.

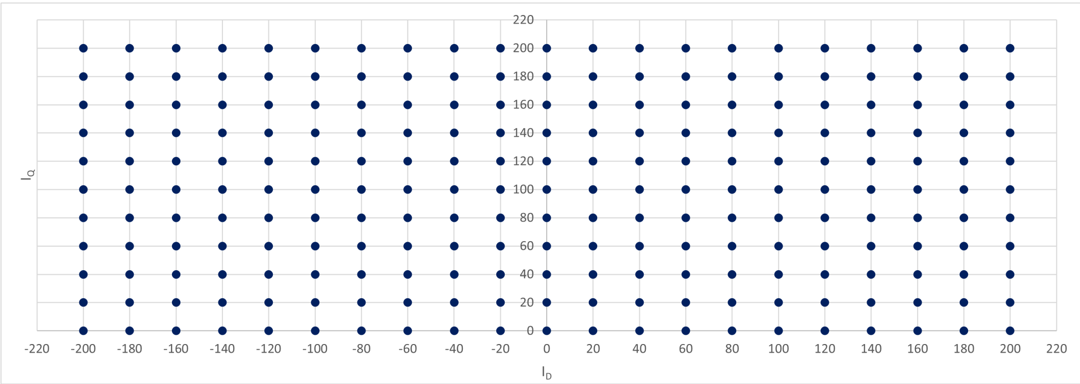

Figure 2.4: DQ axes grid.

In each point, flux linkage waveform of each phase will be computed and saved. At the end of the simulation, each three-phase coordinates data will be transformed in dq coordinates ones, that should be constant value. So there will be a flux value in d axis and a flux value in q axis for every points. Results will be presented as below, in a I_d-λ_d and a I_q-λ_q planes. For the purposes of the algebraic model, the magnetic maps will be represented by two matrices, $[\Lambda_d]$ and $[\Lambda_q]$, in which I_d will change with columns whereas I_q will change with rows.

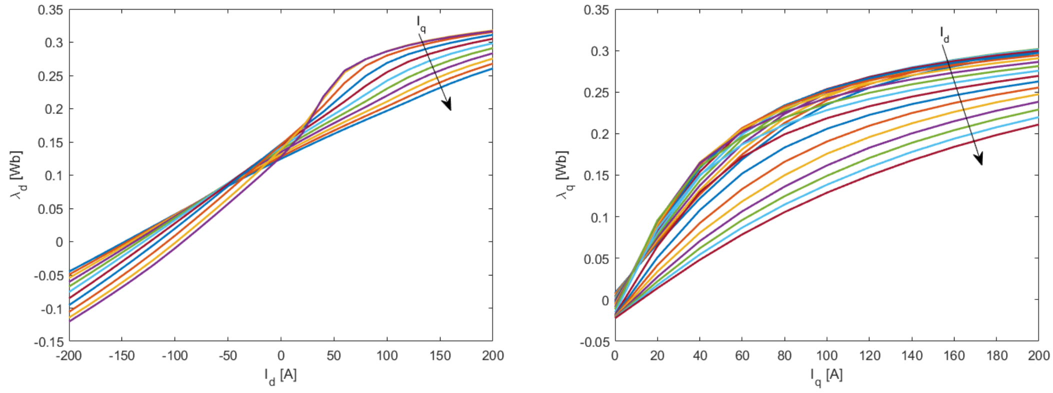

Figure 2.5: Example of flux maps.

2.1.2 Equivalent core-loss resistance identification

Once having FEM model, computing of the last parameter, equivalent iron loss resistance is possible.
As said before, this parameter depends on toque and speed, but in this case a behaviour as illustrated in fig.2.6 is expected.

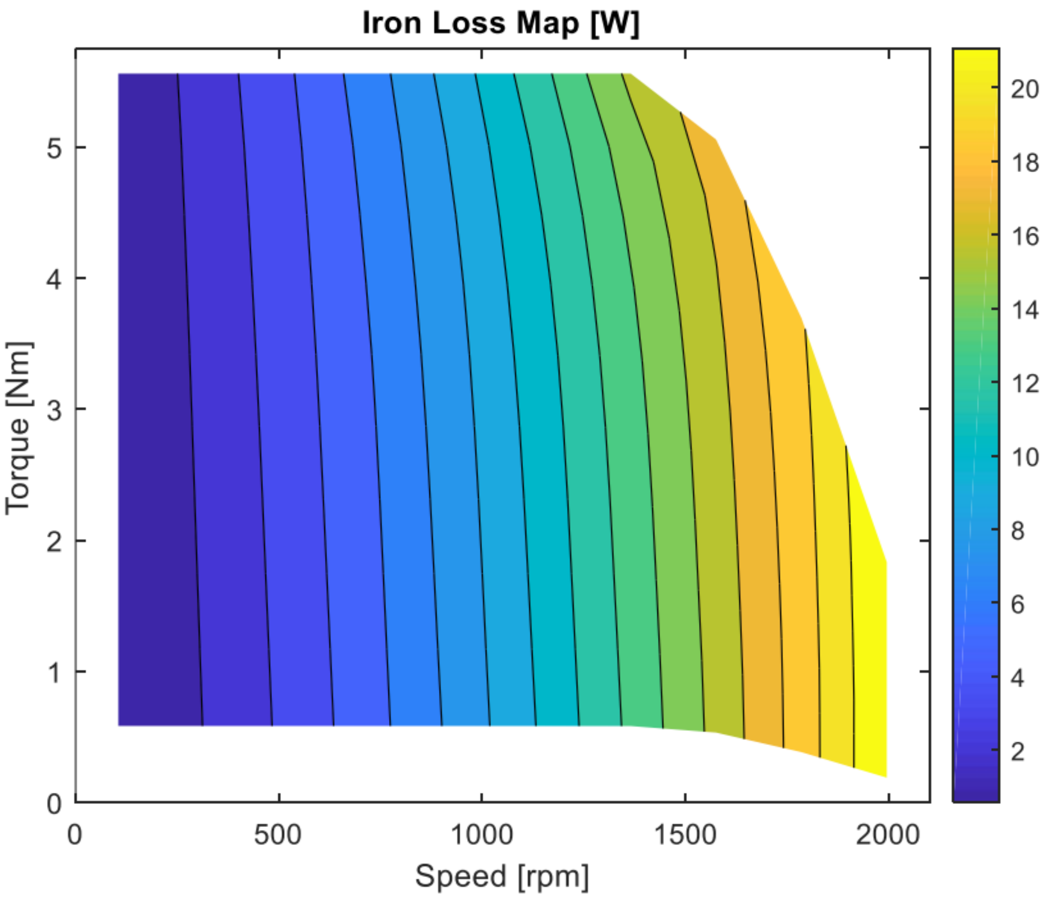

Figure 2.6: Equivalent iron resistance trend for an IPM.

Rather constant resistance trend as function of torque is the effect of a procedure used to compute this map: choosing, for each speed and torque value, the working point with minimal losses.
Obviously, FEM does not provide directly the value of this parameter, so a method to extract it is analyzed.
FEM, in this case, Flux, is able to calculate losses in the stator and rotor iron, but a way to transform these quantities in an equivalent fictitious resistance has to be

described.
As shown in fig.2.2 this equivalent resistance will be in parallel with pilot generator, so its voltage will be V = $\Lambda\omega$. Power dissipated on a resistor is, as in 2.7.[9][10]

$$P = \frac{V^2}{R} \tag{2.7}$$

So to compute these parameter 2.8 will be used.

$$R_{fe} = \frac{(\lambda_d^2 + \lambda_q^2)\omega^2}{P_{fe}} \tag{2.8}$$

2.2 Maximum Torque Per Speed profile

Before moving forward with efficiency map computation, Maximum Torque Per Speed profile have to be calculated. Once having all parameters of the model described before, obtaining the MTPS is very simple. The strength of this method is the computation time at this point of the analysis. After the extrapolation of all parameters by FEM, this algorithm is really fast. Now arbitrary values of the dc-link voltage, the phase current amplitude limit, machine temperature and PM temperature are considered. Varying these inputs it is possible to understand how these conditions affect the efficiency of the machine.
Starting from all parameters described before and voltage and current limit, the MTPS profile is computed, based on the reconstruction of all electromagnetic equations shown in 2.9.

$$\begin{cases} V_{d,eq}^{map} = R_{eq}^{map} I_{d,eq}^{map} - \omega_e \Lambda_q^{map} \\ V_{q,eq}^{map} = R_{eq}^{map} I_{q,eq}^{map} + \omega_e \Lambda_d^{map} \end{cases} \tag{2.9}$$

Where R_{eq}^{map} stands for the equivalent resistance map between the stator resistance and the iron resistance map.
Based on the 2.3 the reconstruction of the stator voltage and the stator current is performed. At this point, if the mechanical losses related to the friction and ventilation are known the torque at the rotor can be computed as in 2.6. Finally, the maximum torque for each speed defines the MTPS according to the voltage and current limit. All working points out of these limits are ruled out. So the working point is acceptable if:

$$V_s^{map} \leq V_s^{max} \;\; \& \;\; I_s^{map} \leq I_s^{max} \tag{2.10}$$

Where V_s^{map} and V_s^{map} are respectively the stator voltage and the stator current in the dq rotating reference frame that represent the peak value of the phase voltage and current. Limits are fixed by the dc-link and voltage source inverter, in particular I_s^{max} is the maximum current of the VSI and V_s^{max} depends on the modulation technique, in this work

$$V_s^{max} = \frac{V_{dc-link}}{\sqrt{3}} \tag{2.11}$$

2.3 Efficiency map

Having every elements described thus far, the computation of the efficiency is easy. Each working point has its iron loss resistance and its current, its stator resistance and its phase current, computed as 2.3, its mechanical losses, so the efficiency is computed as follow:

$$\eta = \frac{T_m \omega_r}{T_m \omega_r + Losses} \tag{2.12}$$

Where

- T_m stands for the shaft torque
- ω_r stands for the shaft speed
- Losses stands for the sum of all losses considered.

In fig. 2.7 an example of efficiency map of the ipm motor is shown

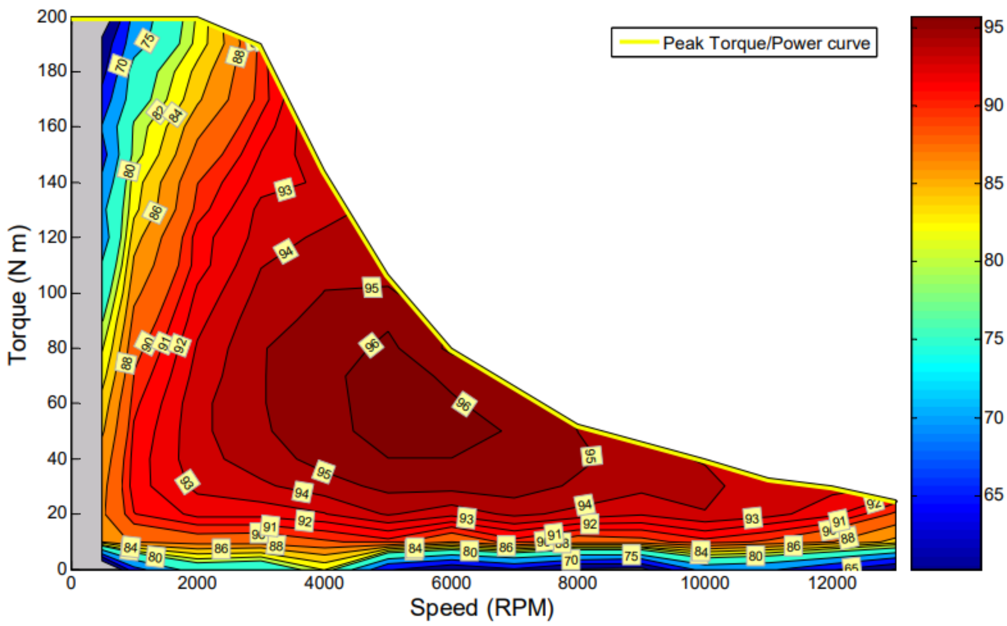

Figure 2.7: Example of efficiency map

It is important to specify that the accuracy of the study depends on the number of point analyzed, if it's low, an interpolation is needed allowing the use of this type of map in a continuous domain.

2.4 Power analysis

When creating efficiency maps, it has to be careful when evaluating losses and the different powers involved. In this algorithm different losses are evaluated in dq rotor coordinates and steady-state conditions. Losses consist of the stator P_{js}, iron losses P_{Fe} and mechanical losses P_{fv}. To be as clear as possible

Phase-domain:

$$P_{js} = 3R_s(\theta_s, f) * I_s^2 \tag{2.13}$$

$$P_{Fe} = 3R_{Fe}(V_s, f) * I_{Fe}^2 \tag{2.14}$$

dq reference frame:

$$P_{js} = \frac{3}{2}R_s(\theta_s, f)|I_s|^2 \tag{2.15}$$

$$P_{Fe} = \frac{3}{2}R_{Fe}(V_s, f)|I_{Fe}|^2 \tag{2.16}$$

Being different reference frames, a definition of the current components is needed: I_s and I_{Fe} are the RMS stator and iron currents in phase domain whereas $\left|\overline{I}_s\right|$ and $\left|\overline{I}_{Fe}\right|$ are the peak values of the current spatial vectors.
With regard to friction and ventilation losses are the same in both references:

$$P_{fv} = T_{fv}\omega_{rm} \tag{2.17}$$

Now all the losses are described. As in 2.18 and in 2.19, the efficiency of IPM machine can be computed for both motoring and generating modes.

$$\eta_{IPM}^{M} = \frac{T_m\omega_r}{T_m\omega_r + \sum P_{loss}} \tag{2.18}$$

$$\eta_{IPM}^{G} = \frac{T_m\omega_r + \sum P_{loss}}{T_m\omega_r} \tag{2.19}$$

Chapter 3

Magnetic model of the electric machine

In this chapter the method used to create magnetic model of the motor will be described. The scope of this part is to establish the correctness of the FEM model, after this point, computation of flux maps will be introduced.
As said before, the analyses to validate this approach were carried out on 2010 Toyota Prius' motor, an IPM V-shaped motor.

3.1 Altair Flux

This work has been done on Flux environment, that is a FEM software by Altair. It is able to simulate magneto static, steady-state and transient conditions, along with electrical and thermal properties. It is a software with 35 years of history during which has become a versatile, efficient and user-friendly tool that helps designers to generate optimized and high-performance products.
The large number of articles on the web in which this machine is analysed gives the possibility to verify that the simulations made on Flux are valid.
Before flux maps are obtained, a number of test are needed to understand whether the model analyzed on Flux is correct. In this chapter each test will be studied.
Flux gives the possibility of drawing the geometric model of the electric machine either directly in the software or importing it from a CAD (dxf files). Autocad was used for convenience as it was more intuitive in drawing.
Once the Autocad project is ready and is imported on Flux, each region of the machine is assigned its own material with magnetic and electric properties. The magnetization direction of the magnet is defined. A first no-load test, without windings, is compute: the air gap flux density test.

3.2 Air gap flux density test

The first test concerns the distribution of the air gap flux. In fig.3.1 the flux density of a pole is shown. It is important to specify that these tests were repeated several times under different conditions as the reference articles, [11] [6], do not specify the temperature conditions to which the results refer. As will be seen in the section on electromotive forces, in fact, the values can be very different depending on the condition of the magnet, being a NdFeB magnets, which has a residual induction that varies greatly with temperature, as shown in 1.4.3.

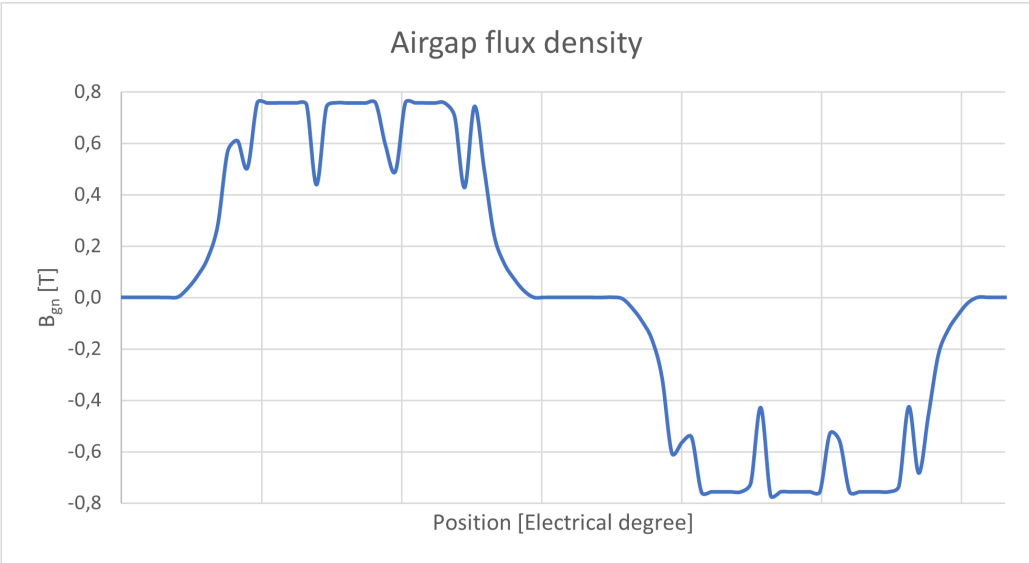

Figure 3.1: Normal air gap flux density

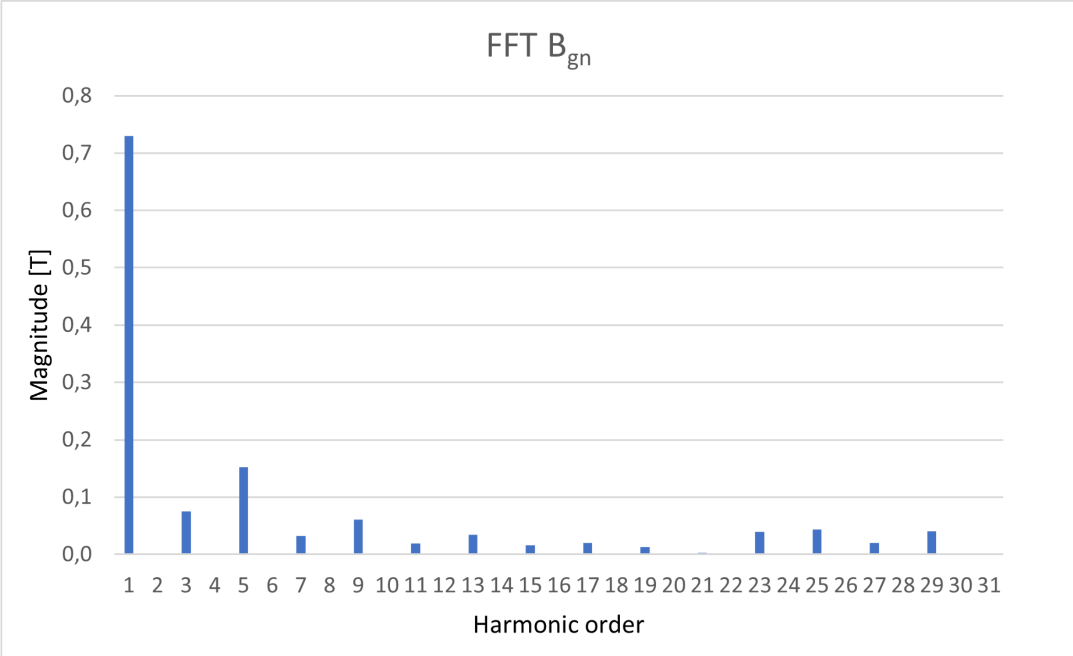

Figure 3.2: Harmonic analysis of the air gap flux density waveform,

Fig.3.2 presents the results of the Fourier transform of the air gap flux density waveform. The magnitude of different harmonics confirm that the rotor geometry is correct. This first test shows whether the geometry of the rotor is right and whether the induction of the magnets is OK, although this will be followed by the next tests, about back emfs at no load.

3.3 Back emf tests

As said before, Not having in detail conditions in which experimental tests on [2] have been computed, in the first test nominal residual induction (at 19 °C) has been considered. As shown in fig. 3.3, back-emf rms value was too high. A second attempt has been done. Normally a good operating temperature value for the stator can be 120 °C, so a test with this value has been computed. As illustrated below, in fig.3.3, correct values of rms back-emf are obtained for a PM temperature of 120°C, so all the following analyses were conducted under these temperature conditions.

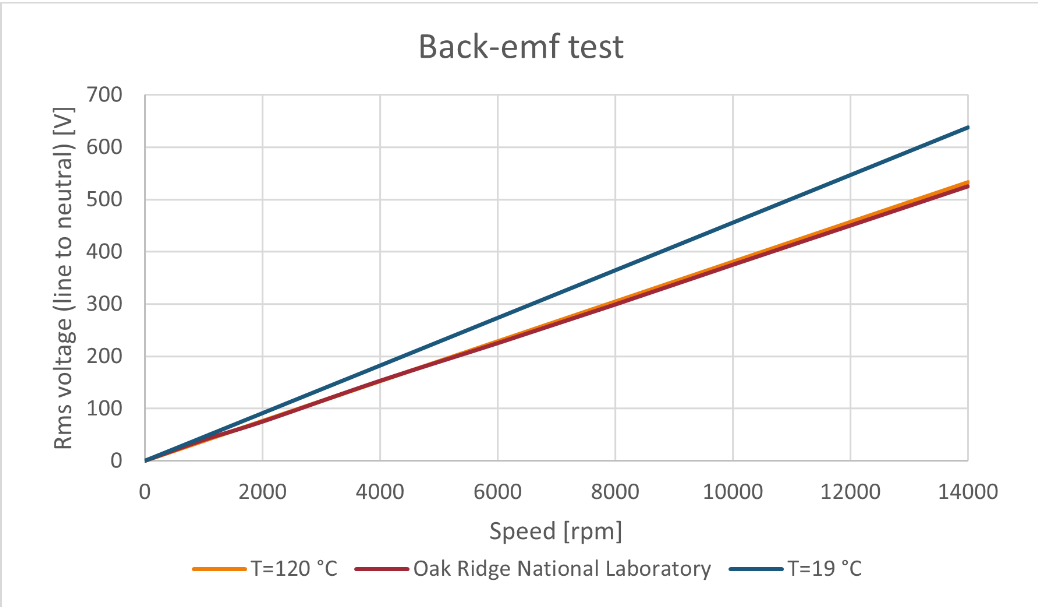

Figure 3.3: RMS voltage value at different speeds.

To be sure that the winding and material of the magnets were described correctly, a reference work based only on the analysis of back-electromotive forces was considered. Following other tests concentrated on this will be shown.
In the next figures abscissa's values are not reported because they are not important in this case. The only important thing is to specify that it is an electrical period, so 90 mechanical degrees.

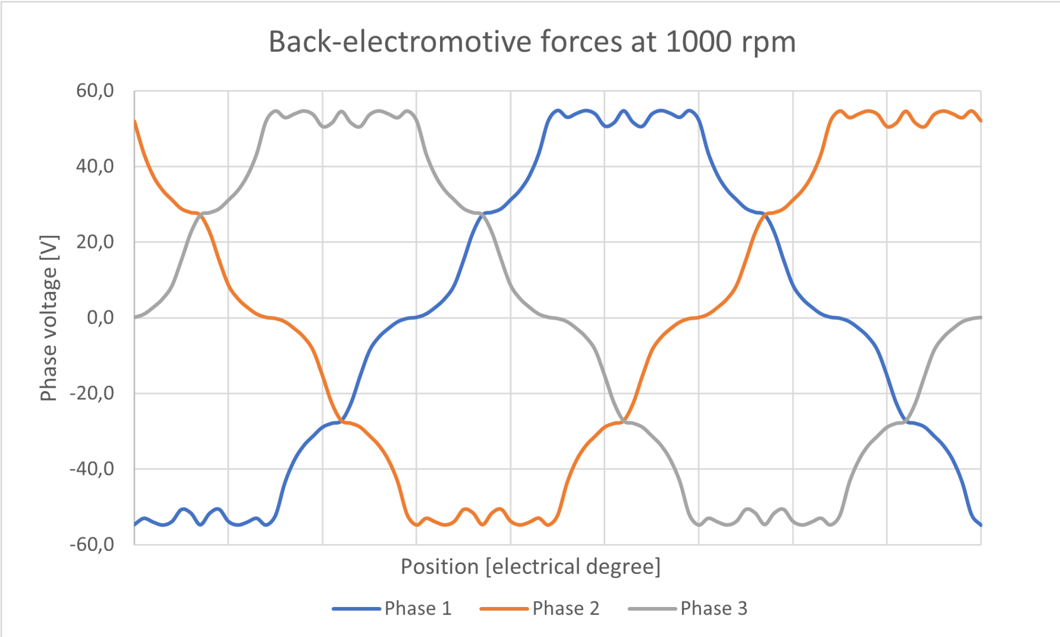

Figure 3.4: Phase back-electromotive forces at 1000 rpm.

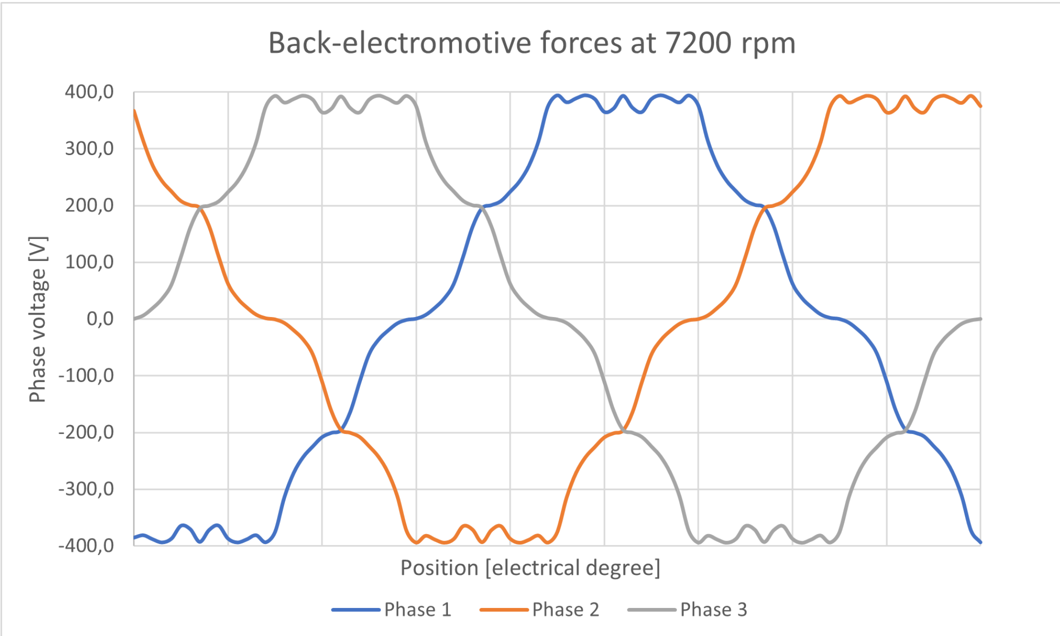

Figure 3.5: Phase back-electromotive forces at 7200 rpm.

The last test, at 3000 rpm shows more information than the other because a Fast Fourier Transform is available. The results are very close to what was shown in [11].

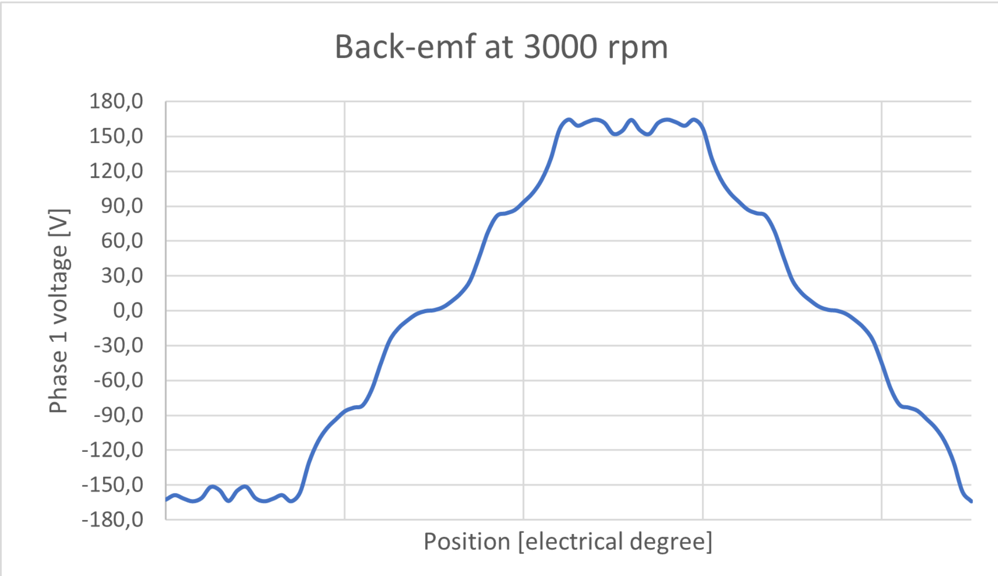

Figure 3.6: Phase 1 back-electromotive force at 3000 rpm.

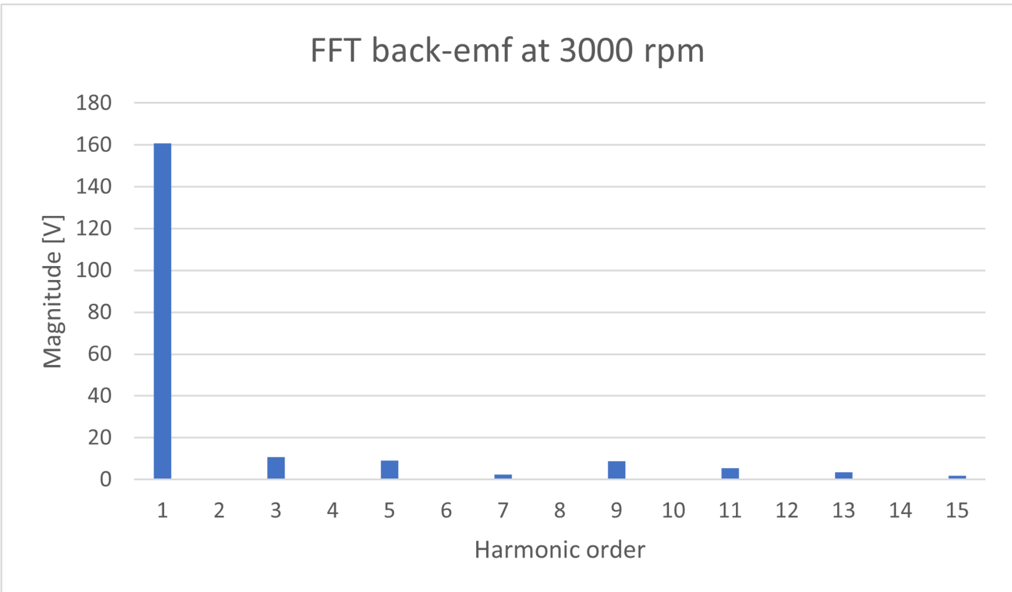

Figure 3.7: Fast Fourier Transform of phase 1 back-emf at 3000 rpm.

3.4 Torque analysis

The last test described in the previous section provides more information than the one already mentioned. Fig. 3.6 shows the phase 1 back-electromotive force waveform, so it makes possible to identify the q axis with respect to the phase 1 axis. Since the electromotive force is shifted by 90 electrical degrees with respect to the flux, d axis position can be found.
Being the first values of the back-emf negative, as shown in fig. 3.8 the angle will be negative in relation to the direction of rotation.

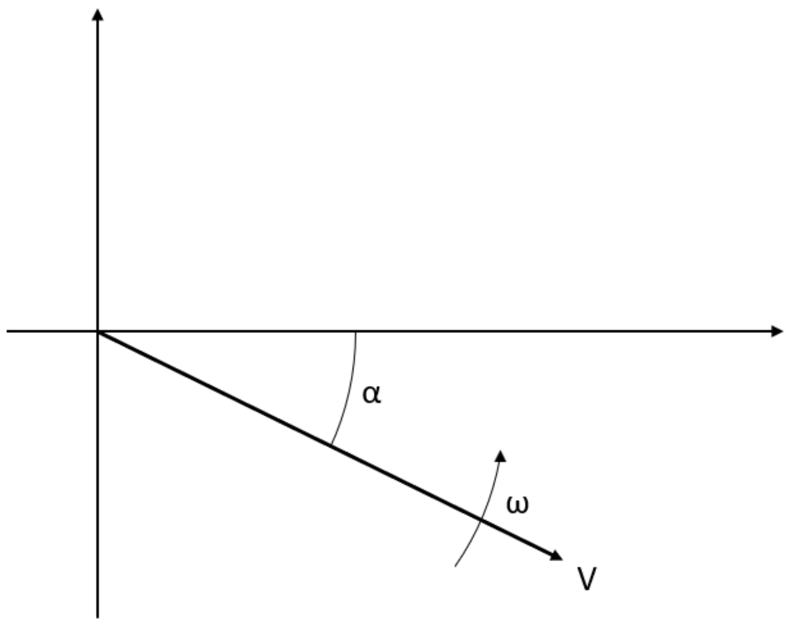

Figure 3.8: Phase shift angle of the back-emf.

Having the phase shift angle, current control in dq axes is possible. The last test to verify the accuracy of the FEM model is partly described in fig.3.9. A current vector in dq axis is provided to the stator thanks to transformations described in chapter 2. Starting from the q axis, the γ angle is varied from 0 to 90 degrees with a constant current module.

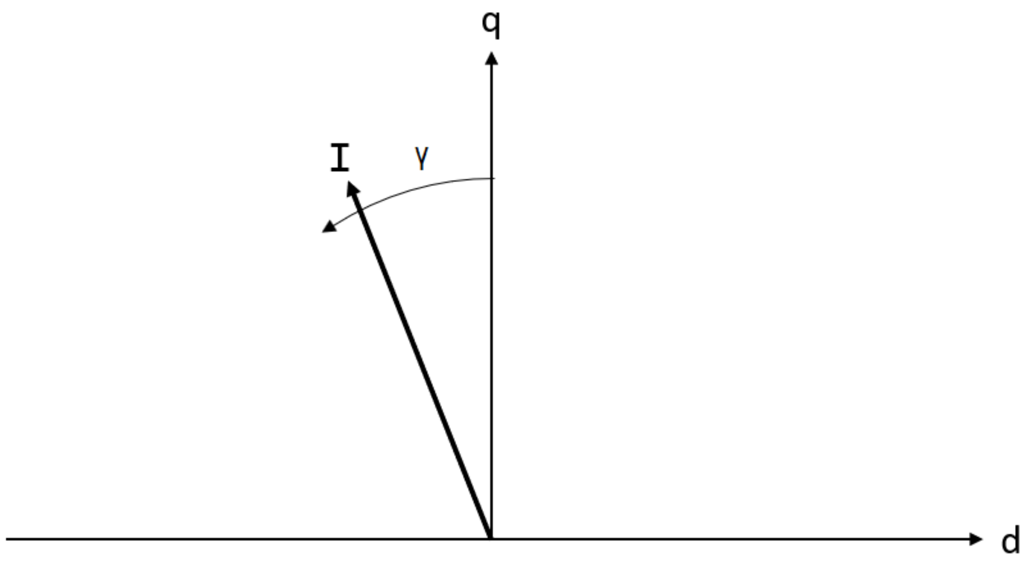

Figure 3.9: dq current control.

Two different simulation conditions have been considered in order to compare the results with two different studies([6] and [11]. In fig.3.10 torque trend at nominal conditions (120 Amps) is shown whereas in fig.3.11 illustrates torque in conditions that are described in [11].

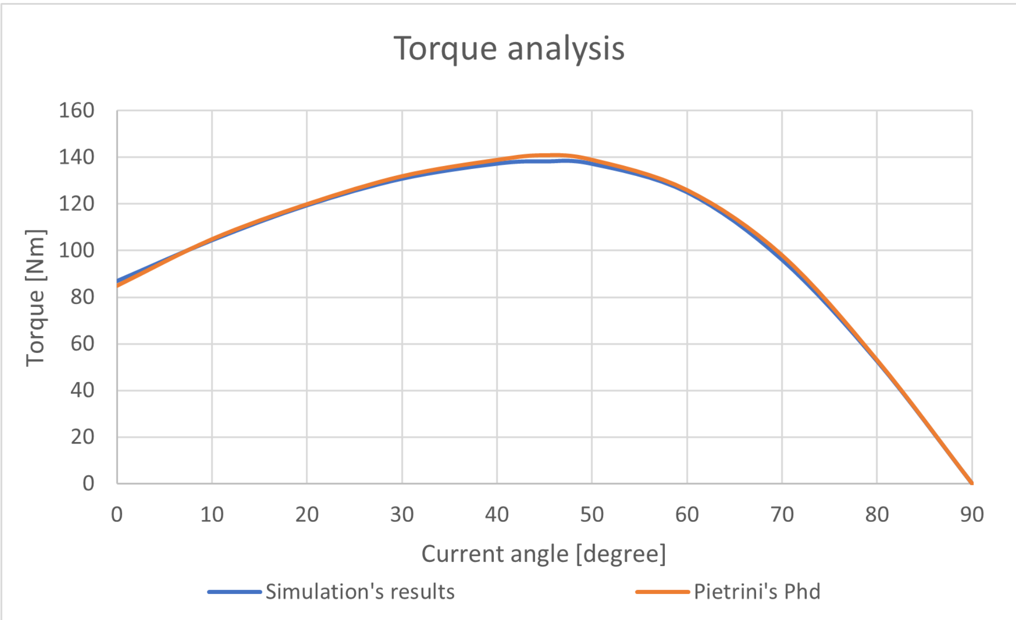

Figure 3.10: Torque at nominal conditions.

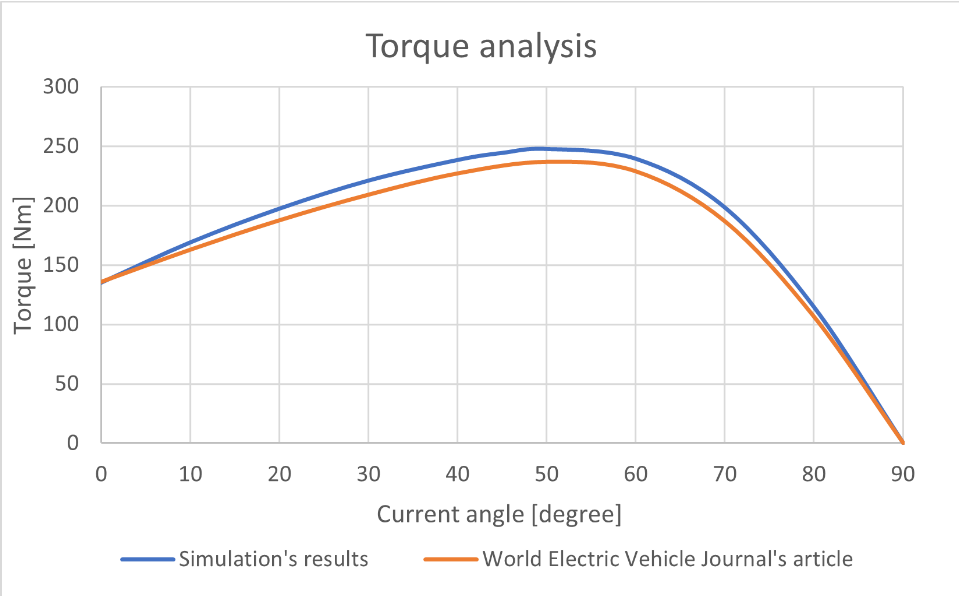

Figure 3.11: Torque with current module I=236Amps.

Chapter 4

FEM Analyses

Once the fem model has been verified, the extrapolation of the flux and iron resistance maps as described in 2 is possible. In this chapter the strategy used to create the maps is illustrated.

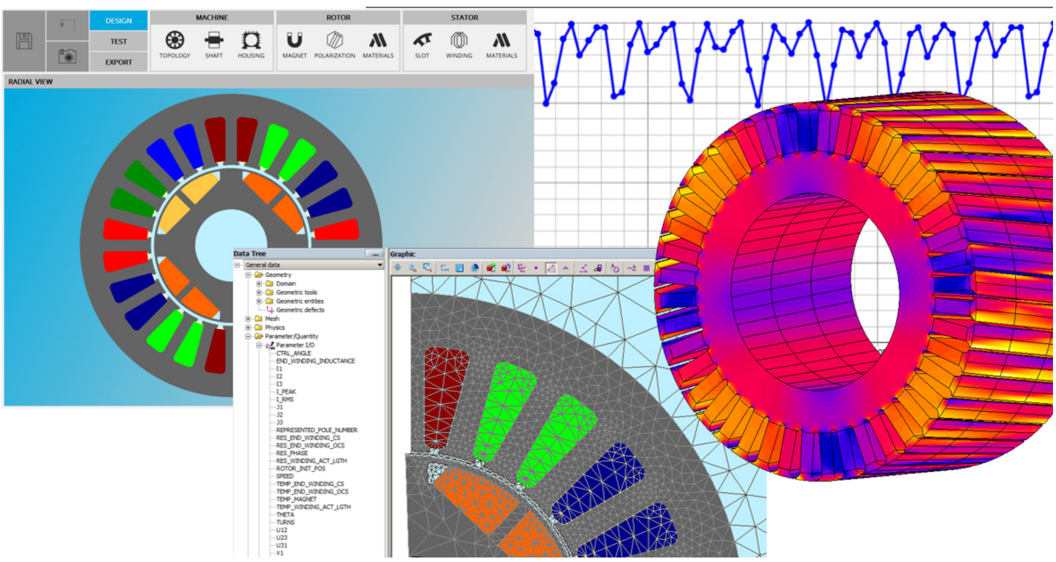

4.1 Flux maps extrapolation

As said in 2 the flux maps extrapolation process consists of a lot of simulations, each one in a different working point. Referring to fig.2.4 an interval of 20 Amps for both currents (I_d and I_q) has been chosen, so an interpolation will be needed to manipulate the data. Starting from the flux waveform, it is important to specify that the strategy described in 2 is valid only for the fundamental harmonic waveform, so a comparison between two different method has been done. For better understanding possible differences between two methods flux wave-forms are shown in fig. 4.1.

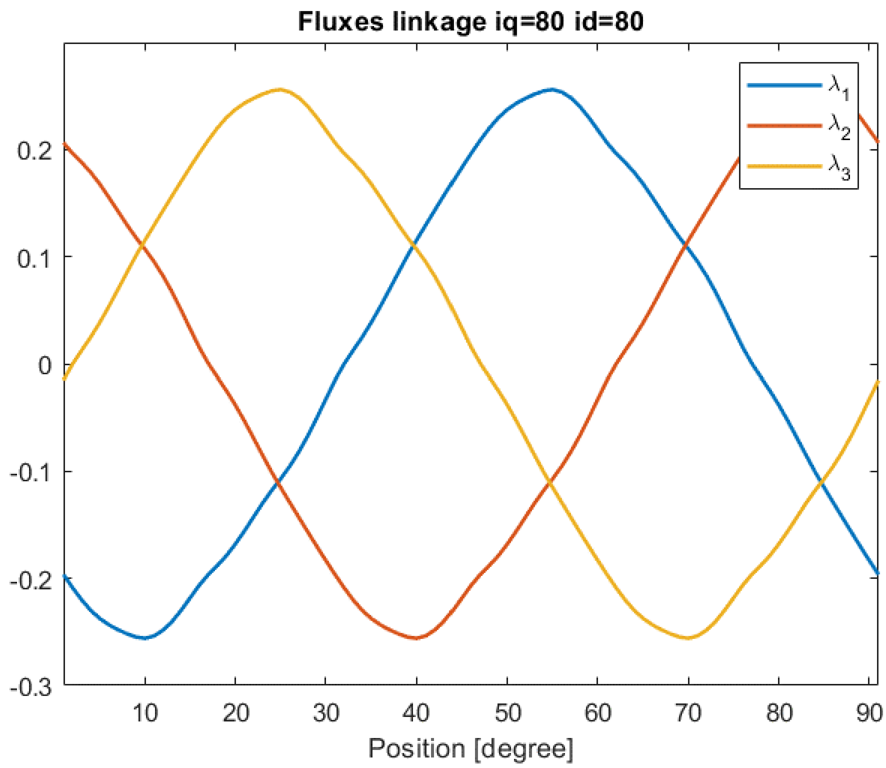

Figure 4.1: Phase fluxes linkage at nominal condition.

It is possible to notice that the wave-forms are not a perfect sinusoidal waveform, but there are harmonics. The presence of these harmonics could be neglected at nominal condition, when the value of the flux is high, but there are different working points in which the flux value is low and these harmonics create a high error in dq flux value computation.
In the first method, all harmonics are considered, so the actual value of the flux

is taken into account for the transformation. In the second method instead, only the fundamental waveform is transformed in dq coordinates. These methods are described in the following sections.

4.1.1 First method

As said before, there are some working points in which each flux wave-forms are affected by several harmonics. Fig. 4.2 shows the flux linkage in phase 1 in zero torque condition, in particular with $I_d = -80Amps$ and $I_q = 0$.

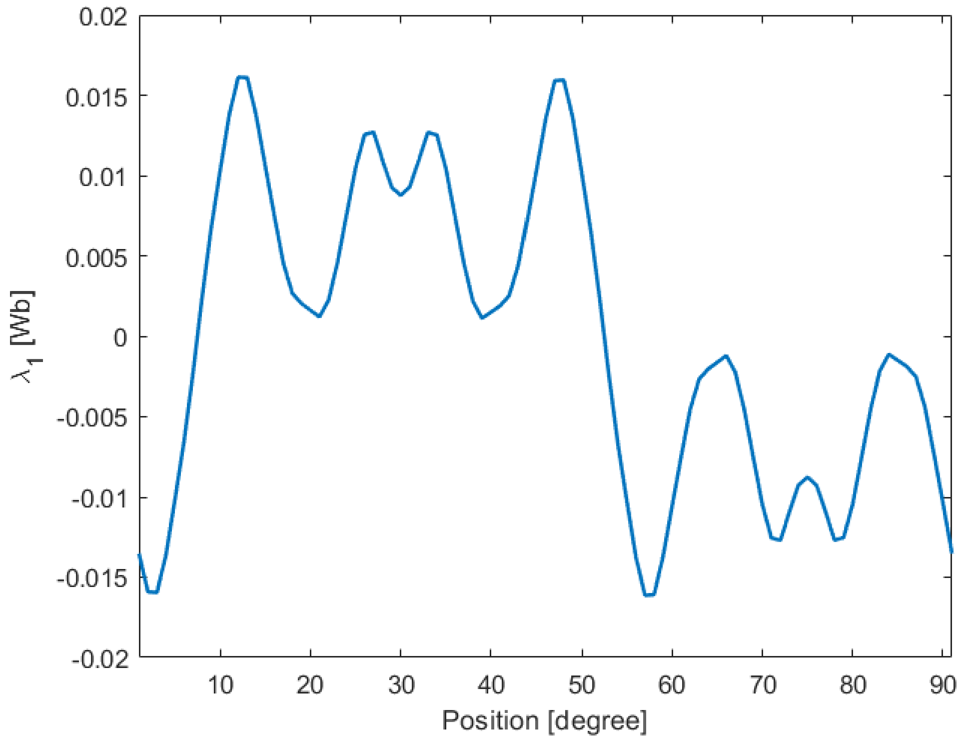

Figure 4.2: Flux linkage in phase 1 at $I_d = -80$ and $I_q = 0$ Amps

Having all flux wave-forms, the three-phase to two-phase transformation is performed point by point. Fig. 4.3 and fig.4.4 show the results of the transformation, the flux trend in dq axis.

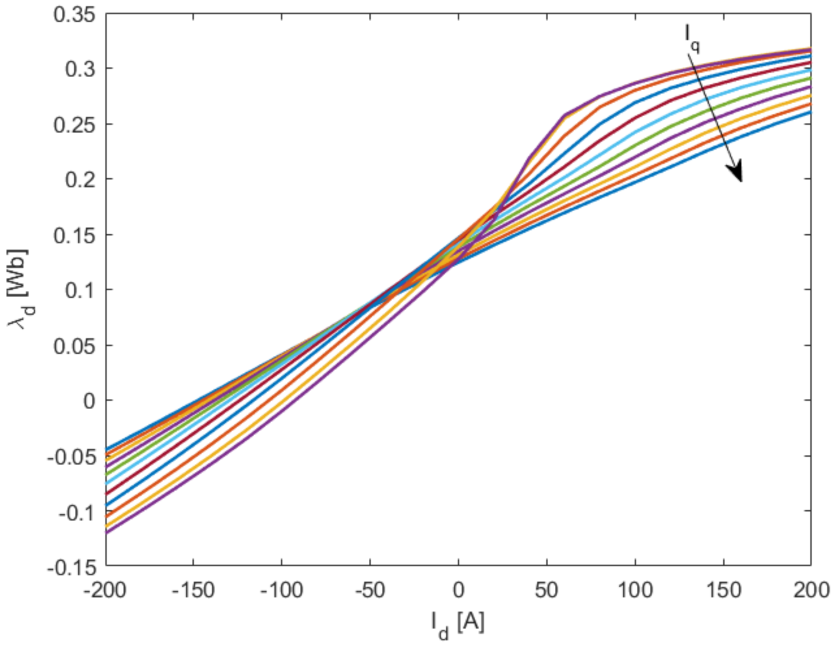

Figure 4.3: Flux in d axis computed by first method.

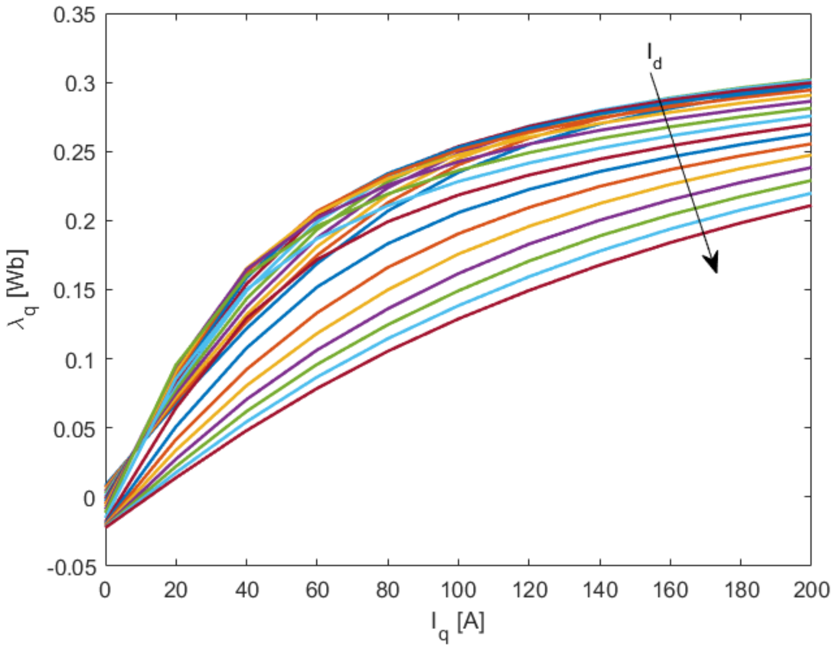

Figure 4.4: Flux in q axes computed by first method.

Obviously, this way of displaying results makes it more difficult to try to find any errors that may exist, as a precise reference is not available. An alternative way is considered: the error was estimated on the torque.
Simulation provides mean torque value in each working point, so computing the torque value according to 4.1 a comparison is possible.

$$T_{em} = \frac{3}{2} p (\Lambda_d I_{eq,q} - \Lambda_q I_{eq,d}) \tag{4.1}$$

Where:

- p is the pole pairs of the machine;
- $I_{eq,d}$ and $I_{eq,q}$ are the coordinates of the grid analyzed.
- Λ_d and Λ_q are the result of the previous analysis.

Fig. 4.5 shows the torque mean values computed by FEM simulations in each working point analysed. As expected for a current I_q=0 the torque is zero.

Simulation torque																					
200	273,4	262,0	249,4	235,8	221,2	206,0	190,2	174,0	157,6	141,2	125,0	109,1	93,7	79,0	65,3	53,1	43,2	36,3	30,6	25,3	20,1
180	267,9	256,7	244,1	230,3	215,5	199,9	183,7	167,0	150,1	133,3	116,5	100,2	84,5	69,6	56,0	44,2	35,5	29,5	24,1	18,9	13,9
160	260,9	249,9	237,5	223,7	208,8	192,9	176,3	159,2	141,9	124,5	107,4	90,7	74,7	59,8	46,3	35,4	28,4	22,9	17,7	12,6	8,2
140	251,5	241,2	229,1	215,4	200,5	184,6	167,8	150,4	132,7	115,0	97,4	80,4	64,3	49,4	36,5	27,2	21,5	16,3	11,2	7,0	3,1
120	238,4	229,2	218,0	204,9	190,3	174,5	157,7	140,3	122,4	104,3	86,6	69,4	53,3	38,7	26,9	19,9	14,7	9,7	5,7	2,1	-1,7
100	219,7	212,1	202,3	190,6	177,0	161,8	145,5	128,3	110,6	92,5	74,7	57,6	41,6	27,8	18,2	12,9	8,1	4,5	1,0	-2,7	-6,1
80	192,8	187,0	179,5	170,0	158,6	145,4	130,3	114,0	96,8	79,2	61,7	44,9	29,5	17,5	10,6	6,5	3,3	0,0	-3,6	-6,7	-9,3
60	155,6	151,9	147,0	140,6	132,3	122,2	110,1	96,1	80,5	64,1	47,6	31,6	17,5	8,5	4,6	2,2	-1,0	-4,3	-7,0	-9,0	-10,5
40	109,6	107,8	105,0	101,1	96,0	89,3	80,9	70,9	59,3	46,3	32,2	18,3	7,1	2,5	1,1	-1,5	-4,3	-6,4	-7,7	-8,6	-9,2
20	56,9	56,2	55,0	53,2	50,8	47,5	43,2	37,7	31,2	24,0	15,9	6,9	0,9	0,4	-1,1	-2,9	-4,1	-4,8	-5,2	-5,4	-5,5
0	-0,1	-0,1	-0,1	0,0	0,0	0,0	0,0	0,0	0,0	0,0	0,0	0,0	0,0	0,0	0,0	0,0	0,0	0,0	0,0	0,0	0,0
	-200	-180	-160	-140	-120	-100	-80	-60	-40	-20	0	20	40	60	80	100	120	140	160	180	200

Figure 4.5: Torque computed by FEM

Fig.4.6 illustrates instead torque value computed using flux maps extrapolated as described before.

Torque 1^{st} method																					
200	302,6	289,7	275,8	261,2	245,8	229,9	213,8	197,4	181,1	165,1	149,4	134,2	119,8	106,2	93,7	82,9	74,6	69,5	65,7	62,5	59,4
180	294,5	281,6	267,7	252,8	237,2	220,9	204,3	187,5	170,7	154,2	138,0	122,5	107,8	94,1	81,7	71,5	64,5	60,3	56,9	53,8	51,2
160	284,8	272,2	258,3	243,3	227,5	211,0	194,0	176,8	159,6	142,6	126,0	110,2	95,2	81,5	69,5	60,2	54,9	51,4	48,3	45,5	43,6
140	272,9	260,8	247,1	232,3	216,4	199,8	182,6	165,1	147,5	130,1	113,3	97,2	82,2	68,6	57,2	49,6	45,8	42,7	39,8	38,1	36,7
120	257,4	246,3	233,4	219,0	203,3	186,8	169,6	152,0	134,3	116,7	99,7	83,5	68,5	55,3	45,2	40,0	37,0	34,2	32,6	31,5	30,3
100	236,4	226,7	215,2	202,0	187,3	171,4	154,6	137,3	119,7	102,1	85,1	69,0	54,3	42,0	34,2	30,9	28,5	27,3	26,2	25,1	24,4
80	207,4	199,4	190,0	178,9	166,3	152,2	136,7	120,2	103,2	86,1	69,5	53,8	39,8	29,5	24,5	22,7	22,0	21,1	20,1	19,6	19,9
60	168,3	162,3	155,4	147,2	137,7	126,6	113,9	99,7	84,3	68,4	52,8	38,1	25,5	18,4	16,8	16,8	16,2	15,5	15,5	16,2	17,6
40	120,9	116,6	111,7	106,0	99,4	91,6	82,5	72,1	60,6	48,1	35,0	22,4	13,0	10,7	11,8	11,8	11,6	12,3	13,7	15,7	18,0
20	67,3	64,0	60,6	56,9	52,9	48,3	43,1	37,2	30,7	23,9	16,7	9,2	5,2	7,3	8,5	9,4	11,1	13,2	15,8	18,5	21,3
0	9,9	7,4	5,2	3,3	1,7	0,4	-0,6	-1,1	-1,2	-0,8	0,0	1,4	3,7	6,5	9,2	12,0	14,9	17,8	20,7	23,6	26,6
	-200	-180	-160	-140	-120	-100	-80	-60	-40	-20	0	20	40	60	80	100	120	140	160	180	200

Figure 4.6: Torque computed using the first method.

It is easy to notice that there is a significant error between two values, in particular in working point with zero current in q axis, point at high currents and in general at all the points belonging to the first quadrant. This is explained because the flux linkage at those points is not sinusoidal at all, but is affected by many harmonics.
Fig.4.7 shows the order of magnitude of the error at all the points. Errors at zero current in q axis were not taken into account because being a condition of zero torque, the error would have been orders of magnitude larger .

Percent error 1^{st} method																					
200	10,7	10,6	10,6	10,8	11,1	11,6	12,4	13,5	14,9	16,9	19,5	23,1	27,8	34,4	43,6	56,2	72,9	91,4	114,6	147,1	195,6
180	9,9	9,7	9,7	9,8	10,0	10,5	11,2	12,3	13,7	15,7	18,5	22,3	27,6	35,1	46,1	61,8	81,6	104,2	135,8	184,5	269,6
160	9,2	8,9	8,8	8,8	9,0	9,4	10,0	11,0	12,4	14,5	17,4	21,5	27,5	36,4	50,1	70,0	93,4	124,4	173,5	262,5	431,6
140	8,5	8,1	7,9	7,8	7,9	8,2	8,8	9,7	11,1	13,2	16,3	20,8	27,8	38,9	56,7	82,3	113,0	162,3	256,9	446,6	1068,6
120	8,0	7,4	7,1	6,9	6,9	7,1	7,5	8,4	9,7	11,9	15,1	20,3	28,7	43,2	67,9	101,4	150,9	253,6	468,5	1414,3	1678,6
100	7,6	6,9	6,3	6,0	5,8	5,9	6,2	7,0	8,2	10,4	13,9	19,8	30,6	51,4	88,3	140,2	251,2	503,8	2476,8	831,0	301,4
80	7,6	6,6	5,8	5,2	4,8	4,7	4,9	5,4	6,6	8,7	12,5	19,7	34,9	68,5	132,0	252,0	556,7	52102,9	453,7	192,0	114,7
60	8,2	6,9	5,7	4,8	4,0	3,6	3,4	3,7	4,6	6,7	10,9	20,3	45,7	116,8	262,5	673,2	1577,1	258,9	120,8	78,9	67,9
40	10,3	8,2	6,4	4,9	3,6	2,6	1,9	1,7	2,2	4,0	8,7	22,8	83,8	324,9	962,3	699,7	170,6	93,7	77,7	82,2	95,4
20	18,1	13,9	10,2	7,0	4,2	1,8	0,1	1,4	1,8	0,5	5,1	32,5	478,8	1734,4	650,8	221,0	170,0	176,8	204,8	243,3	290,0
0	-	-	-	-	-	-	-	-	-	-	-	-	-	-	-	-	-	-	-	-	-
	-200	-180	-160	-140	-120	-100	-80	-60	-40	-20	0	20	40	60	80	100	120	140	160	180	200

Figure 4.7: Percent error in each working point.

4.1.2 Second Method

At the contrary of the first method, the second one considers only the fundamental harmonic, so it is based on the Fourier principle. A Fast Fourier Transform is needed. In this case, Flux gives the possibility to extract the FFT directly in an Excel file where Amplitude and phase of each harmonic is specified.
Fig. 4.8 allows an easy interpretation of what has been said so far. As in the previous section, blue waveform represents the real flux linkage in a phase, the red one is the first order harmonic, the fundamental one.

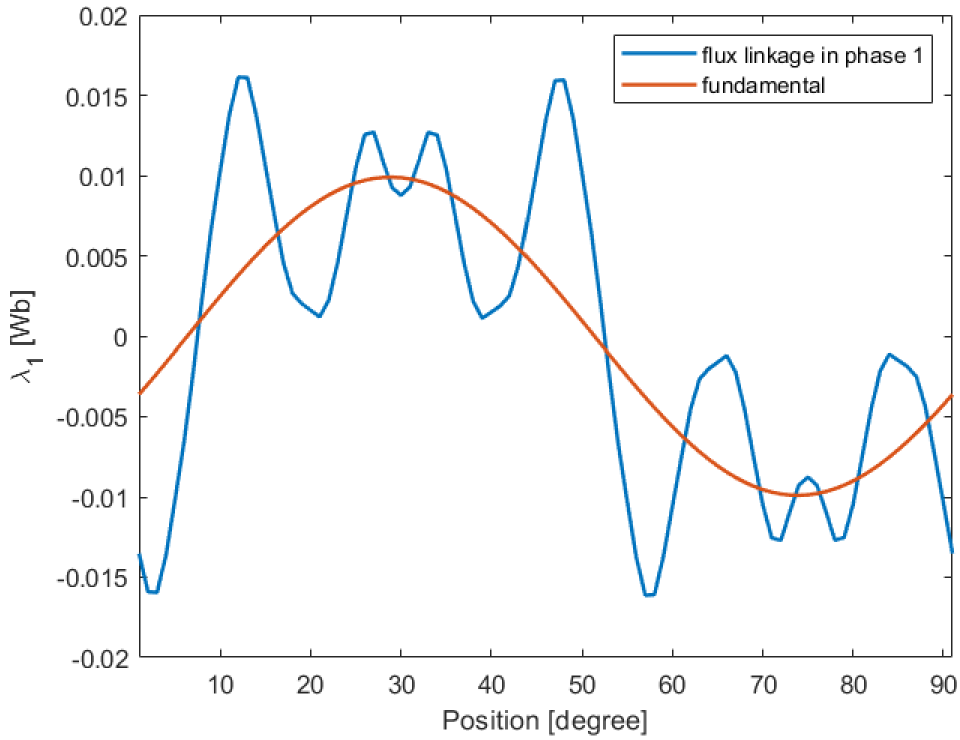

Figure 4.8: Fundamental harmonic of flux linkage.

A part of MATLAB code used to obtain the fundamental is described above.

```


//%take amplitude and phase value of the flux linkage in phase 1
    lambda_max_1=cell2mat(readcell('fft_flusso1_iq0.xls','Sheet',flusso1,'Range','C20:C20'));
    phase_1=cell2mat(readcell('fft_flusso1_iq0.xls','Sheet',flusso1,'Range','E20:E20'));
    l1(:,i)=cell2mat(readcell('flusso1_iq0.xls','Sheet',k1,'Range','C16:C106'));


    //%take amplitude and phase value of the flux linkage in phase 2
    lambda_max_2=cell2mat(readcell('fft_flusso2_iq0.xls','Sheet',flusso2,'Range','C20:C20'));
    phase_2=cell2mat(readcell('fft_flusso2_iq0.xls','Sheet',flusso2,'Range','E20:E20'));
    l2(:,i)=cell2mat(readcell('flusso2_iq0.xls','Sheet',k2,'Range','C16:C106'));


    //%take amplitude and phase value of the flux linkage in phase 3
    lambda_max_3=cell2mat(readcell('fft_flusso3_iq0.xls','Sheet',flusso3,'Range','C20:C20'));
    phase_3=cell2mat(readcell('fft_flusso3_iq0.xls','Sheet',flusso3,'Range','E20:E20'));
    l3(:,i)=cell2mat(readcell('flusso3_iq0.xls','Sheet',k3,'Range','C16:C106'));


    //%creation of fundamental waveform


    for c=1:91
        lambda1(c,i)=lambda_max_1*cos(4*c*pi/180+phase_1);
        lambda2(c,i)=lambda_max_2*cos(4*c*pi/180+phase_2);
        lambda3(c,i)=lambda_max_3*cos(4*c*pi/180+phase_3);
    end
```

Listing 4.1: Code to extract fundamental waveform.

In the first part, phase and harmonic amplitude values are extracted by the excel file. With these information it is possible to derive the waveform.
Fig. 4.9 and fig. 4.10 show the results of this method, but as already seen before, the method was validate by torque error.

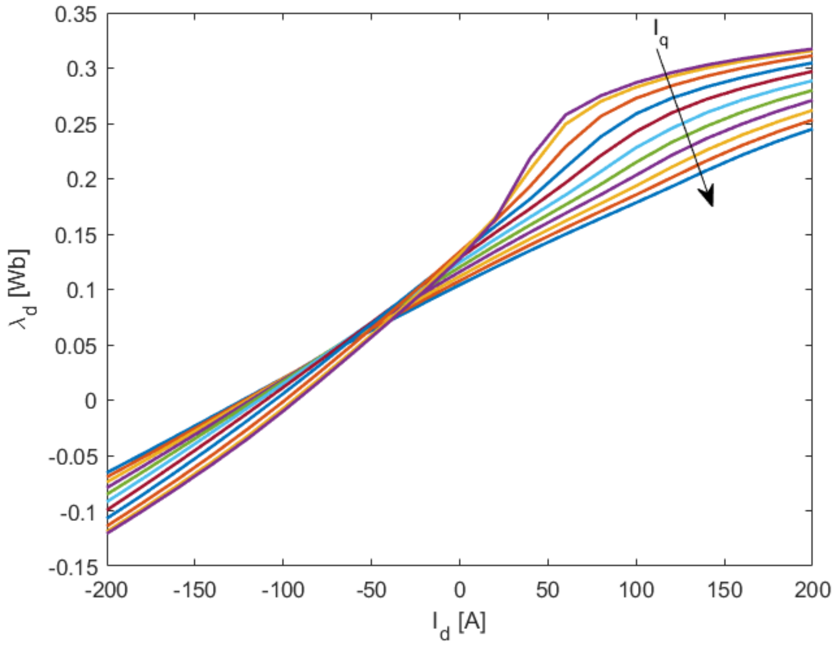

Figure 4.9: Flux in d axes computed by second method.

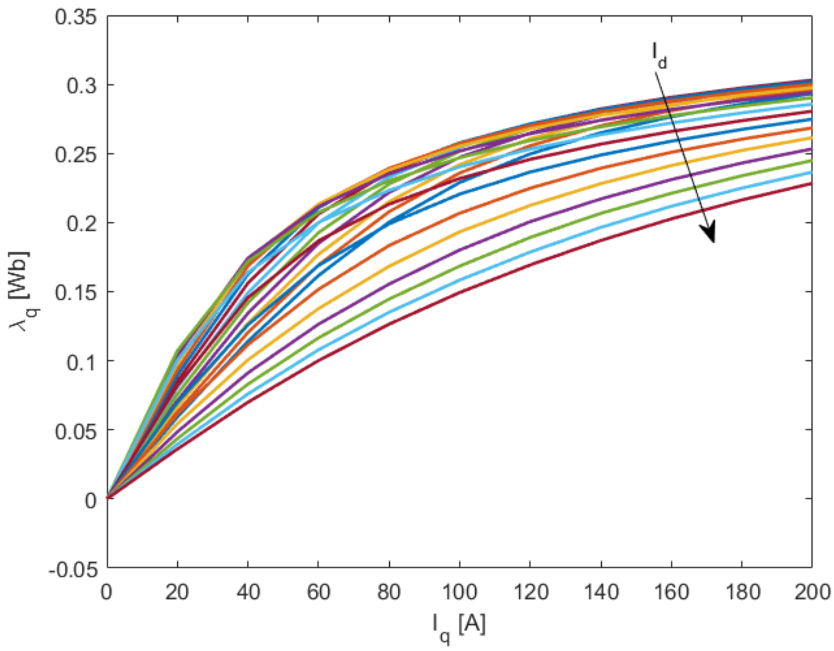

Figure 4.10: Flux in q axes computed by second method.

Fig.4.11 shows the mean value of the torque computed using 4.1 and flux maps computed using this method.

Torque 2nd method																					
200	273,3	261,9	249,3	235,6	221,1	205,9	190,1	173,9	157,5	141,1	124,9	109,0	93,6	79,0	65,2	53,0	43,1	36,3	30,5	25,2	20,0
180	267,8	256,5	243,9	230,2	215,4	199,8	183,6	166,9	150,1	133,2	116,5	100,2	84,4	69,6	55,9	44,2	35,5	29,4	24,1	18,8	13,9
160	260,7	249,8	237,3	223,5	208,6	192,8	176,2	159,2	141,8	124,5	107,3	90,6	74,7	59,7	46,3	35,3	28,3	22,8	17,6	12,5	8,2
140	251,4	241,0	228,9	215,3	200,4	184,5	167,7	150,3	132,6	114,9	97,4	80,4	64,3	49,4	36,5	27,2	21,5	16,3	11,1	7,0	3,1
120	238,3	229,1	217,8	204,7	190,1	174,4	157,6	140,2	122,3	104,3	86,5	69,4	53,2	38,6	26,9	19,8	14,7	9,7	5,7	2,1	-1,7
100	219,6	212,0	202,2	190,5	176,9	161,7	145,4	128,2	110,5	92,5	74,6	57,5	41,6	27,7	18,1	12,8	8,1	4,6	1,0	-2,7	-6,1
80	192,7	186,9	179,4	169,9	158,5	145,3	130,3	113,9	96,8	79,2	61,7	44,9	29,5	17,5	10,5	6,4	3,3	-0,1	-3,6	-6,8	-9,2
60	155,5	151,8	146,9	140,5	132,2	122,1	110,0	96,1	80,5	64,1	47,5	31,6	17,5	8,5	4,6	2,1	-1,0	-4,3	-7,0	-9,1	-10,5
40	109,6	107,7	104,9	101,1	95,9	89,3	80,9	70,8	59,2	46,2	32,2	18,2	7,1	2,5	1,1	-1,5	-4,3	-6,4	-7,8	-8,7	-9,3
20	56,9	56,2	55,0	53,2	50,7	47,5	43,1	37,7	31,2	23,9	15,8	6,9	0,9	0,4	-1,2	-3,0	-4,1	-4,8	-5,2	-5,4	-5,5
0	-0,1	-0,1	-0,1	-0,1	-0,1	-0,1	0,0	0,0	0,0	0,0	0,0	0,0	0,0	0,0	0,0	0,0	0,0	0,0	0,0	0,0	0,0
	-200	-180	-160	-140	-120	-100	-80	-60	-40	-20	0	20	40	60	80	100	120	140	160	180	200

Figure 4.11: Torque computed using the second method.

The torque values are more similar to those shown in fig.4.5. In particular, this evidence is clear in zero current in q axis working points and in that point where the current module is higher.
In fact, as in fig.4.12, percent error is negligible in all working point of the grid. Again, the error at zero torque points has not been taken into account as even with values very close to zero, as shown in fig.4.11, the error can have very high values.

Percent error 2nd method																					
200	0,06	0,05	0,06	0,06	0,06	0,05	0,06	0,06	0,07	0,07	0,05	0,04	0,04	0,03	0,02	0,13	0,07	0,09	0,17	0,14	0,64
180	0,06	0,05	0,06	0,06	0,06	0,06	0,06	0,06	0,06	0,07	0,05	0,04	0,04	0,03	0,05	0,01	0,10	0,26	0,28	0,56	0,33
160	0,07	0,07	0,06	0,06	0,06	0,06	0,07	0,06	0,07	0,06	0,06	0,05	0,05	0,07	0,05	0,16	0,38	0,31	0,27	0,15	0,02
140	0,06	0,06	0,07	0,06	0,07	0,06	0,07	0,06	0,07	0,06	0,06	0,05	0,06	0,04	0,08	0,20	0,24	0,04	0,18	0,10	1,27
120	0,06	0,06	0,07	0,07	0,06	0,07	0,07	0,07	0,07	0,06	0,06	0,05	0,07	0,08	0,20	0,25	0,14	0,16	0,32	0,05	0,01
100	0,06	0,06	0,06	0,07	0,07	0,07	0,07	0,07	0,07	0,07	0,07	0,07	0,10	0,13	0,27	0,41	0,20	0,86	1,32	0,29	0,09
80	0,05	0,05	0,06	0,07	0,07	0,08	0,07	0,08	0,07	0,08	0,08	0,10	0,11	0,20	0,37	0,13	0,48	27,13	0,43	0,83	0,30
60	0,02	0,04	0,06	0,06	0,07	0,08	0,09	0,09	0,09	0,09	0,10	0,13	0,17	0,38	0,37	1,55	3,71	0,41	0,19	0,51	0,12
40	0,04	0,03	0,04	0,05	0,06	0,08	0,09	0,10	0,11	0,13	0,14	0,18	0,36	0,89	2,56	1,88	0,72	0,85	0,54	0,34	0,84
20	0,07	0,07	0,07	0,08	0,09	0,10	0,11	0,13	0,14	0,17	0,20	0,31	2,40	6,76	2,36	1,10	1,00	0,77	0,53	0,80	0,43
0	-	-	-	-	-	-	-	-	-	-	-	-	-	-	-	-	-	-	-	-	-
	-200	-180	-160	-140	-120	-100	-80	-60	-40	-20	0	20	40	60	80	100	120	140	160	180	200

Figure 4.12: Percent error in each working point.

It is important to specify that there aren't reference values for comparing the correctness of these two methods, in fact, obtained results have been compared with the torque computed by simulations, not real data. From a theoretical point of view, the second method is more accurate so the results of the latter will be taken into account.

4.2 Iron resistance map computation

As explained in Chapter 2, once having FEM model computing of equivalent iron resistance maps is possible. In particular Altair Flux gives the possibility to compute the losses easily. Before talking about the computation, it is good to remember the dependence of iron losses on the speed, but they also depend on the flux in the machine, so they change if the currents change. To obtain a more accuracy equivalent resistance map, several simulations are computed.
A simulation in each working point of the second quadrant of the grid ($I_d \leq 0$) for each speed value has been computed. The second quadrant has been chosen because being an IPM motor, the second quadrant is where the motor will be controlled and for saving computation time and simulations memory. In this case, having the results of these simulations, 13 different losses maps are available, one for each chosen speed value. As said in 2, having loss maps it is possible to compute the iron resistance map using 4.2.

$$R_{fe} = \frac{(\lambda_d^2 + \lambda_q^2)\omega^2}{P_{fe}} \tag{4.2}$$

where:

- λ_d and λ_q are extract by flux maps;
- ω depends on speed and it is:

$$\omega = \frac{2\pi pn}{60} \tag{4.3}$$

where:

- n stands for the rotor speed;
- p stands for poles pair of the machine.

Now 13 iron resistance maps are available, one for each speed value. The scope is to create a map that illustrates how iron resistance changes in a torque-speed plane. The used method is to compute total losses (iron and copper losses) in each point analyzed at each speed for different given torque values (number of these points depends on the accuracy of the method), and take into account the point where minimal losses are computed. In this work a value of torque in an interval of 20Nm has been considered.
Fig.4.13 shows the result of the method explained. As expected, equivalent iron resistance is approximately constant with the torque and varies with speed.

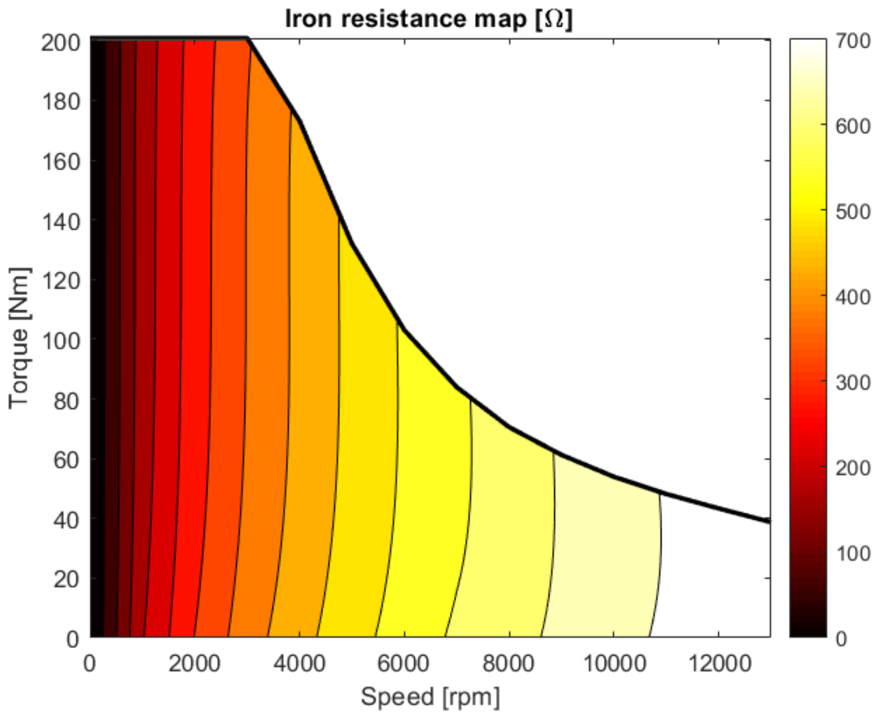

Figure 4.13: Equivalent iron resistance map.

Chapter 5

Algebraic model

The scope of this chapter is to describe the procedure used to compute efficiency maps. Before talking of efficiency the Maximum Torque Per Ampere and Maximum Torque Per Speed have to be evaluated.
Some initial considerations have to be done: in the efficiency study there are some terms that were not considered because there was no way to accurately obtain the value of some losses. In detail, these terms are mechanical losses, skin effect in conductors and switching losses.

5.1 MTPA and MTPS profiles

5.1.1 MTPS profile

Maximum Torque Per Speed profile is a curve that describe the maximum values of torque the motor can provide to the shaft. In other words, this curve defines the range of possible working point on the T-ω plane.
As explained in 2 the procedure to extract this curve is really straightforward. Having all inputs and parameters of the algebraic model described up this point voltage and current limits are defined in relation with the inverter. In each working point of the grid in I_d-I_q plane torque value has been computed. Voltage in d and q axis is computed as in 5.1:

$$\begin{cases} V_{d,eq}^{map} = R_{eq}^{map} I_{d,eq}^{map} - \omega_e \Lambda_q^{map} \\ V_{q,eq}^{map} = R_{eq}^{map} I_{q,eq}^{map} + \omega_e \Lambda_d^{map} \end{cases} \tag{5.1}$$

where R_{eq} is the parallel resistance between phase resistance and equivalent iron resistance computed in Chapter 4, so it depends on the speed. The next step is to compute current and voltage module, if it is higher than the limits analyzed point is not a working point, so it is out of the MTPS. At the end only the points in which torque is the highest are taken into account, this points represent the MTPS curve. A part of code to select MTPS point is illustrated before, in particular the point at 2000 rpm of speed is shown.

```


for q=1:11
    for d=1:11
        coppia=3*p*((flusso_d_fondamentale(q,d)*iq(q))-(flusso_q_fondamentale(q,d)*id(d)))/2;
        current=sqrt(id(d)^2+iq(q)^2);
        Vd_eq=Rs_2000(q,d)*id(d)-omega(2)*flusso_q_fondamentale(q,d);
        Vq_eq=Rs_2000(q,d)*iq(q)+omega(2)*flusso_d_fondamentale(q,d);
        Vs_d=(Rs_2000(q,d)+R_fe_2000(q,d))/R_fe_2000(q,d)*Vd_eq;
        Vs_q=(Rs_2000(q,d)+R_fe_2000(q,d))/R_fe_2000(q,d)*Vq_eq;
        V=sqrt(Vs_d^2+Vs_q^2);
        if(current>Imax)
            coppia=0;
        end
        if(V>Vmax)
            coppia=0;
        end
        if(coppia>MTPS(2))
            MTPS(2)=coppia;
        end
    end
end
```

Listing 5.1: Code to extract fundamental waveform.

Fig.5.1 shows the results of the procedure described. This trend can be explained by the fact that non-interpolated maps were taken into account for the calculation of this curve. In fig.5.2 MTPS curve obtained with interpolated maps is shown. It is clear that non-interpolated maps introduce an error.

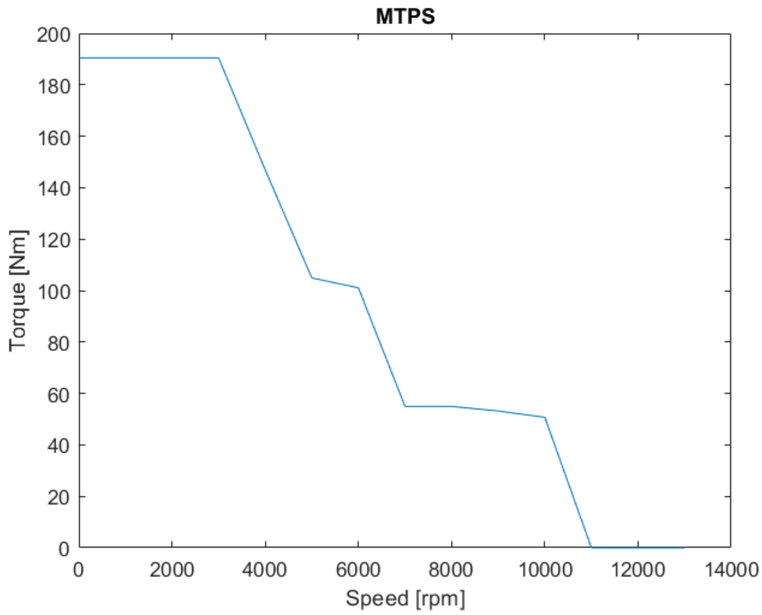

Figure 5.1: MTPS profile without interpolation.

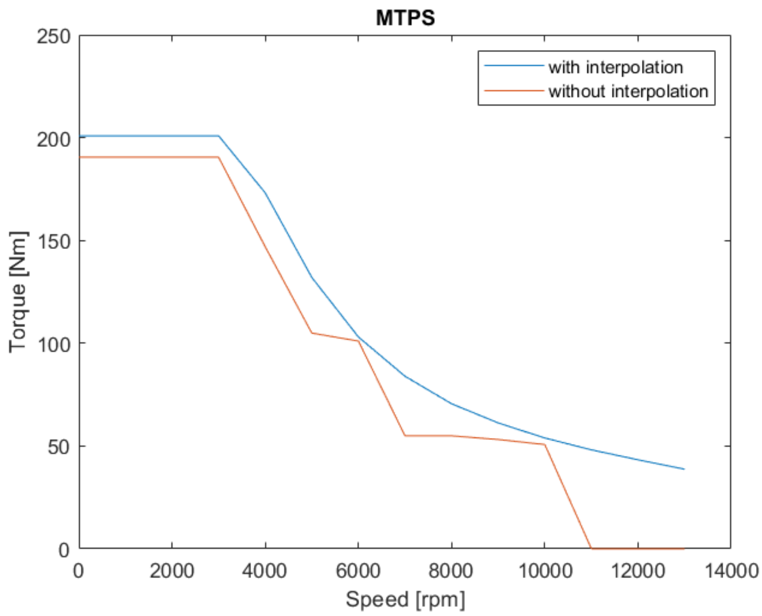

Figure 5.2: MTPS profiles.

5.1.2 MTPA profile

Maximum Torque Per Ampere is a characteristic curve of the motor, it depends on the geometry. As its name suggests, it consists of all point at which a certain torque is obtained with the minimum current value. Fig.5.3 and fig.5.4 show the MTPA profile of the IPM motor analyzed. A code that describes how MTPA profile has been computed is shown below.

```
T_analysed=linspace(0,250,51);
Id_vect=id;
T_temp=contourc(Id_vect,iq,coppia,T_analysed);

i=1;
step=1;
index=0;
id=zeros(length(T_analysed),length(T_temp(1,:)));
iq=zeros(length(T_analysed),length(T_temp(1,:)));

while i<=length(T_analysed)
    while T_temp(1,step)==T_analysed(i)
        index=T_temp(2,step);
        id_temp=T_temp(1,step+1:step+index);
        iq_temp=T_temp(2,step+1:step+index);
        id(i,:)=[id_temp nan*ones(1,length(T_temp(1,:))-length(id_temp))];
        iq(i,:)=[iq_temp nan*ones(1,length(T_temp(1,:))-length(iq_temp))];
        if (step+index)<=length(T_temp)
            step=step+index+1;
            i=i+1;
        end
        if step>length(T_temp(1,:))
            break;
        end
    end
end

// MTPA creation
idq=hypot(id,iq);
A=0;
ind=0;
for j=1:length(T_analysed)
    [A,ind]=min(idq(j,:));
    Id_MTPA(j)=id(j,ind);
    Iq_MTPA(j)=iq(j,ind);
    Is_MTPA(j)=idq(j,ind);
end
```

Listing 5.2: Code to extract MTPA profile.

Fig.5.3 illustrates this curve obtained with torque values extracted by simulations, whereas fig.5.4 is computed thanks to flux maps using the second method described before. Each figure shows two different curve: the trend of the red one is given by the fact that a discrete method is used, the blue one is the interpolation of the latter. Both curves are represented for further proof of the correctness of method 2.

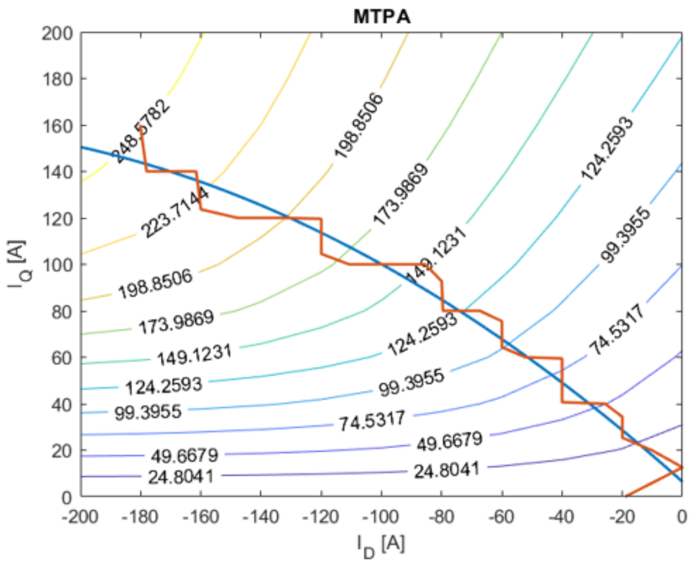

Figure 5.3: MTPA profile by simulation data.

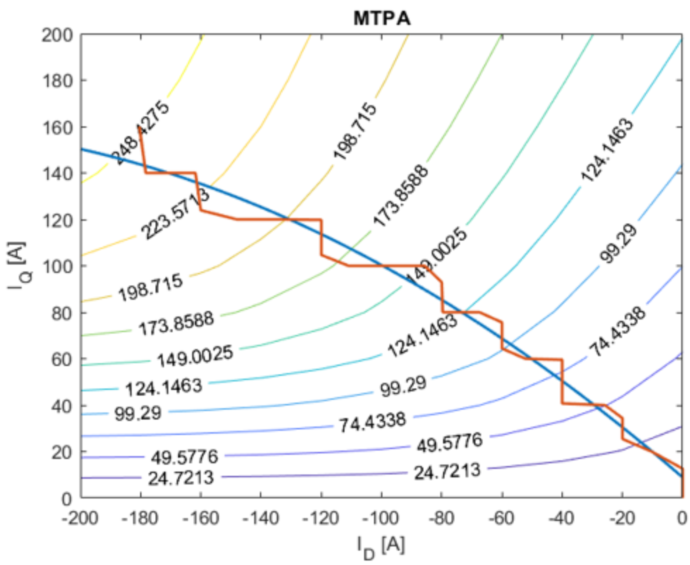

Figure 5.4: MTPA profile by computation of flux maps.

5.2 Efficiency map

At this point of the analysis, all parameters and inputs are available to compute the efficiency maps of the machine. In a first time, only two terms of losses were considered: iron losses and the copper ones. The method used to compute the efficiency in each working point is partially reported in 2. Basically, starting from the equivalent circuit shown in fig.5.5 and considering the point chosen to extract the equivalent iron resistance, $I_{s,d}$,$I_{s,q}$,$I_{Fe,d}$ and $I_{Fe,q}$ can be computed as in 5.2.

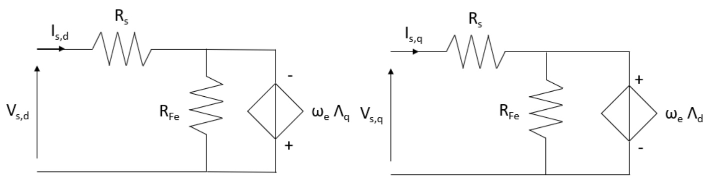

Figure 5.5: Equivalent circuit in dq coordinates.

$$\overline{I}_{Fe} = \overline{V}_s \frac{1}{R_s + R_{Fe}} - \overline{I}_{eq} \frac{R_s R_{Fe}}{R_s + R_{Fe}} \tag{5.2}$$

Now, having quantities in dq coordinates a coefficient of $\frac{3}{2}$ must be entered for the calculation of the losses as in 5.3 and in 5.4.

$$P_{js} = \frac{3}{2} R_s(\theta_s, f) |I_s|^2 \tag{5.3}$$

$$P_{Fe} = \frac{3}{2} R_{Fe}(V_s, f) |I_{Fe}|^2 \tag{5.4}$$

Considering only the terms described above, the efficiency can be computed as follow.

$$\eta = \frac{T_m \omega_r}{T_m \omega_r + \sum P_{loss}} \tag{5.5}$$

```
for s=1:13
    for t=1:201
        %circuit model
         Rs_eq=(R*rfe(t,s))/(R+rfe(t,s));
         q=index_q(t,s);
         d=index_d(t,s);
         T=3*p*((flusso_d_interp(q,d)*iq(q)-(flusso_q_interp(q,d)*id(d))))/2;
         is=sqrt(id(d)^2+iq(q)^2);
         Vd_eq=Rs_eq*id(d)-omega(s)*flusso_q_interp(q,d);
         Vq_eq=Rs_eq*iq(q)+omega(s)*flusso_d_interp(q,d);
         Vs_d=((Rs_eq+abs(rfe(t,s)))*Vd_eq/abs(rfe(t,s)));
         Vs_q=((Rs_eq+abs(rfe(t,s)))*Vq_eq/abs(rfe(t,s)));
         V=sqrt(Vs_d^2+Vs_q^2);
         Ife_d=-(id(d)*Rs_eq/(Rs_eq+rfe(t,s)))+(Vd_eq/(Rs_eq+rfe(t,s)));
         Ife_q=-(iq(q)*Rs_eq/(Rs_eq+rfe(t,s)))+(Vq_eq/(Rs_eq+rfe(t,s)));
         ife=sqrt(Ife_d^2+Ife_q^2);
         is_d=id(d)+Ife_d;
         is_q=iq(q)+Ife_q;

         //computing different mechanical losses trend that will be take into account for the efficiency computation
         meccaniche(1,s)=(1e-7*(omega(s)/p)^3+0.00001*(omega(s)/p)^2+0.43*(omega(s)/p));
         meccaniche_1(1,s)=(1e-6*(omega(s)/p)^3+0.00006*(omega(s)/p)^2+0.43*(omega(s)/p));
         meccaniche_2(1,s)=(5e-7*(omega(s)/p)^3+0.00003*(omega(s)/p)^2+0.43*(omega(s)/p));
         perdite_totali(t,s)=(3/2)*R*(is_d^2+is_q^2)+(3/2)*rfe(t,s)*ife^2+meccaniche_2(1,s);
%         perdite_totali(t,s)=0.0000006*(is_d^2+is_q^2)*(omega(s)/p)^2+(3/2)*R*(is_d^2+is_q^2)+(3/2)*rfe(t,s)*ife^2+meccaniche(1,s);

         pout=T*omega(s)/p;
         efficiency(t,s)=(T*omega(s)/p)/((T*omega(s)/p)+perdite_totali(t,s));

    end
end
```

Listing 5.3: Efficiency map code.

Fig.5.6 shows the result of integration of efficiency value and MTPS profile, the efficiency map of the machine. It is clear that this map cannot be considered reliable because the region with an efficiency value higher than 96% is too large.

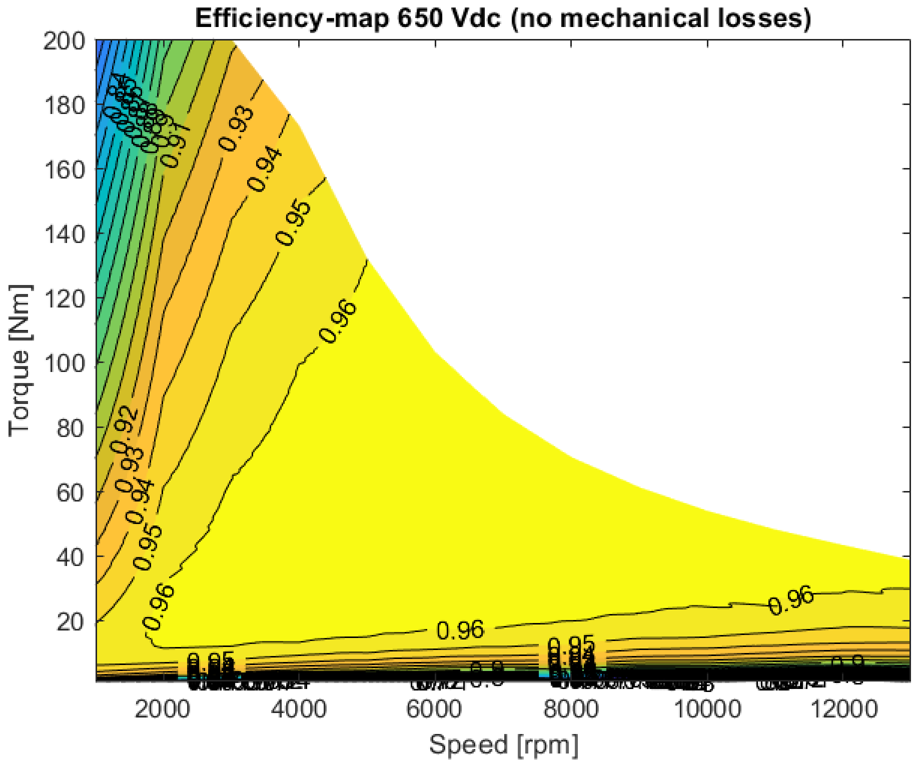

Figure 5.6: Efficiency map with 650 Vdc and no mechanical losses.

Fig.5.7 in the next page shows the value of efficiency in some working points, chosen to allow a comparison with reference values in [2]. A comparison with reference values has been made to understand why the results differ so much from the references. Fig.5.8 shows the percent error of the results in related with the reference values.

Efficiency on the T-ω plane

200	0,7998	0,8857											
180	0,8193	0,8974	0,9263										
160	0,8384	0,9086	0,9341										
140	0,8564	0,9188	0,9410	0,9521									
120	0,8724	0,9276	0,9468	0,9562									
100	0,8877	0,9356	0,9518	0,9596	0,9639								
80	0,9020	0,9430	0,9565	0,9627	0,9660	0,9679							
60	0,9167	0,9501	0,9607	0,9653	0,9675	0,9688	0,9692						
40	0,9318	0,9568	0,9640	0,9668	0,9677	0,9683	0,9680	0,9675	0,9672	0,9664			
20	0,9485	0,9626	0,9654	0,9659	0,9652	0,9640	0,9625	0,9610	0,9594	0,9577	0,9561	0,9545	0,9528
	1000	2000	3000	4000	5000	6000	7000	8000	9000	10000	11000	12000	13000

Figure 5.7: Efficiency values without mechanical losses.

Efficiency percent error without mechanical losses

200	12,48	7,42											
180	8,46	5,84	2,30										
160	4,58	3,70	2,04										
140	4,25	2,04	1,70	1,79									
120	3,71	1,68	1,25	1,59									
100	2,55	1,56	1,03	1,00	1,44								
80	2,00	1,33	0,68	0,70	0,62	1,33							
60	1,82	1,59	1,11	0,86	0,77	0,91	1,47						
40	2,34	2,28	1,97	1,53	0,80	0,86	1,35	1,60	2,29	2,73			
20	4,59	4,42	4,71	3,72	2,61	3,52	2,34	3,22	3,06	2,37	2,73	3,61	2,85
	1000	2000	3000	4000	5000	6000	7000	8000	9000	10000	11000	12000	13000

Figure 5.8: Percent error of efficiency without mechanical losses.

It is possible to notice there is a high error in working point at high speed and low torque. This deviation may be due to mechanical losses because in these points they are prevalent. different mechanical loss trends belonging to machines similar to the one analysed and operating in the same applications were taken into account as mechanical loss trends tp check whether this deviation is due to the method or the simplifications made. Fig.5.9 show the trend of mechanical losses as a function of speed, modeled as polynomial.

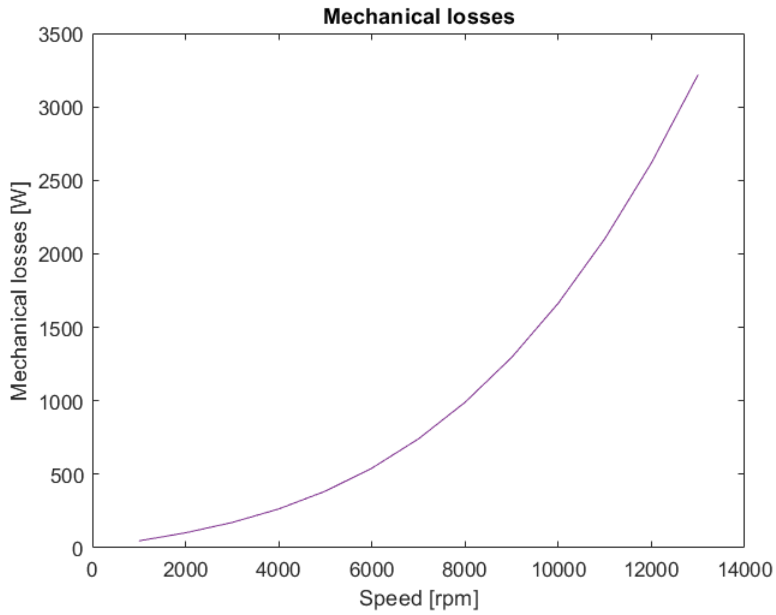

Figure 5.9: First Mechanical losses trend that has been considered.

Fig.5.10 shows the resulting map with assumed mechanical losses.

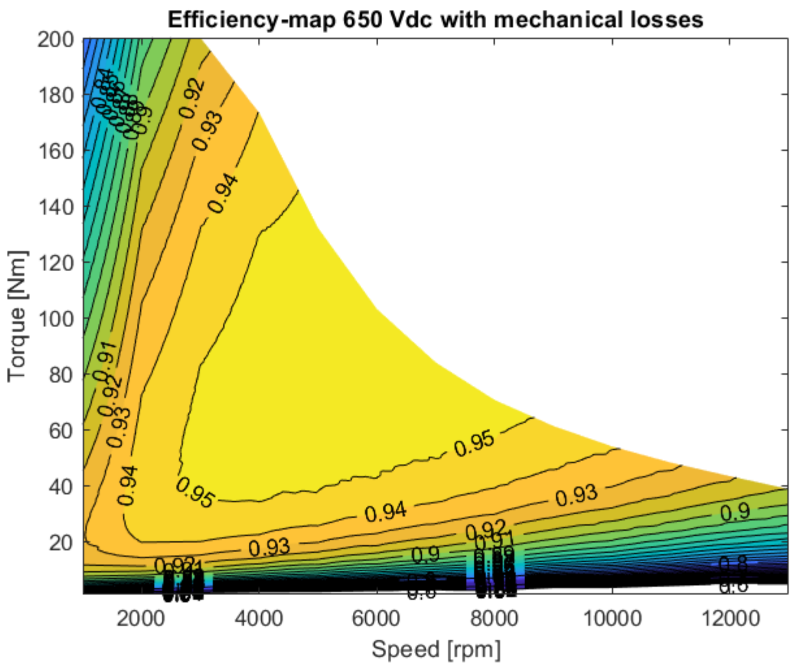

Figure 5.10: Efficiency map considering the first trend of mechanical losses.

Efficiency on the T-ω plane with first mechanical losses

200	0,7983	0,8838											
180	0,8177	0,8953	0,9237										
160	0,8365	0,9061	0,9311										
140	0,8541	0,9159	0,9376	0,9480									
120	0,8695	0,9241	0,9427	0,9515									
100	0,8842	0,9314	0,9469	0,9539	0,9572								
80	0,8975	0,9377	0,9503	0,9555	0,9576	0,9579							
60	0,9105	0,9429	0,9524	0,9557	0,9563	0,9556	0,9538						
40	0,9223	0,9459	0,9516	0,9525	0,9511	0,9489	0,9453	0,9410	0,9367	0,9313			
20	0,9294	0,9412	0,9414	0,9381	0,9329	0,9264	0,9189	0,9105	0,9014	0,8915	0,8811	0,8700	0,8585
	1000	2000	3000	4000	5000	6000	7000	8000	9000	10000	11000	12000	13000

Figure 5.11: Efficiency values considering first trend of mechanical losses.

Efficiency percent error with first mechanical losses

200	12,31	7,22											
180	8,28	5,62	2,02										
160	4,36	3,43	1,73										
140	3,99	1,74	1,34	1,37									
120	3,39	1,31	0,82	1,10									
100	2,17	1,11	0,52	0,41	0,75								
80	1,51	0,76	0,03	0,05	0,25	0,31							
60	1,15	0,84	0,25	0,14	0,39	0,46	0,13						
40	1,33	1,16	0,70	0,05	0,94	1,17	1,02	1,16	0,89	0,93			
20	2,63	2,26	2,27	0,86	0,76	0,39	2,30	2,14	3,18	4,88	5,56	5,75	4,84
	1000	2000	3000	4000	5000	6000	7000	8000	9000	10000	11000	12000	13000

Figure 5.12: Percent error of efficiency considering first mechanical losses trend.

Seeing the error in low torque working points a better trend at low speed has been shown. For this reason it is realistic to think that this is the right direction, so some iron losses estimations had been considered varying polynomial coefficients. Decreasing polynomial coefficient a smoother trend of mechanical losses is obtained.

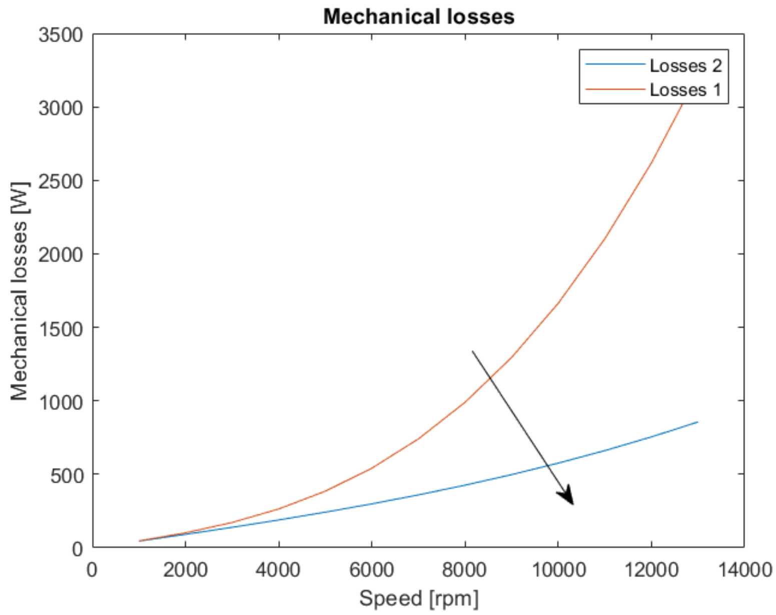

Figure 5.13: Second Mechanical losses trend that has been considered.

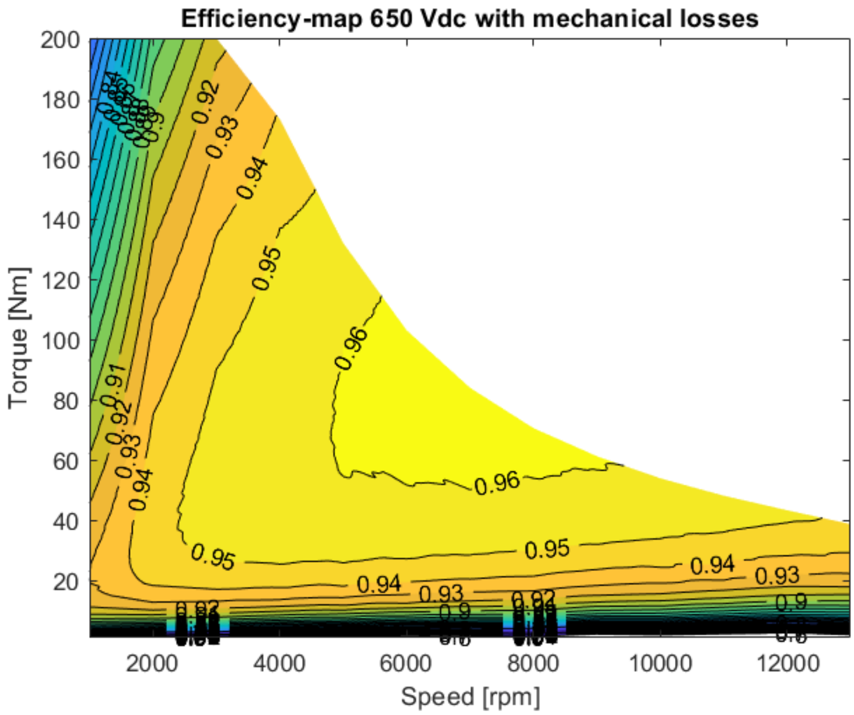

Figure 5.14: Efficiency map considering the second trend of mechanical losses.

Now the central region of the map shows a reliable trend compared to what could be the real one.

Efficiency on the T-ω plane with second mechanical losses

200	0,7984	0,8840											
180	0,8177	0,8955	0,9242										
160	0,8366	0,9064	0,9317										
140	0,8541	0,9162	0,9382	0,9492									
120	0,8696	0,9245	0,9435	0,9528									
100	0,8843	0,9318	0,9479	0,9555	0,9596								
80	0,8977	0,9382	0,9515	0,9576	0,9607	0,9624							
60	0,9107	0,9437	0,9540	0,9584	0,9604	0,9615	0,9617						
40	0,9226	0,9470	0,9540	0,9565	0,9572	0,9575	0,9569	0,9559	0,9552	0,9539			
20	0,9301	0,9434	0,9459	0,9458	0,9446	0,9429	0,9408	0,9386	0,9362	0,9337	0,9312	0,9285	0,9258
	1000	2000	3000	4000	5000	6000	7000	8000	9000	10000	11000	12000	13000

Figure 5.15: Efficiency values considering second trend of mechanical losses.

Efficiency percent error with second mechanical losses

200	12,32	7,24											
180	8,28	5,64	2,08										
160	4,37	3,46	1,79										
140	3,99	1,77	1,41	1,50									
120	3,40	1,35	0,90	1,24									
100	2,18	1,16	0,62	0,57	1,01								
80	1,52	0,82	0,16	0,16	0,07	0,77							
60	1,18	0,92	0,42	0,14	0,04	0,15	0,69						
40	1,37	1,27	0,94	0,47	0,30	0,26	0,19	0,41	1,07	1,46			
20	2,69	2,48	2,73	1,67	0,49	1,37	0,09	0,92	0,66	0,14	0,12	0,91	2,78
	1000	2000	3000	4000	5000	6000	7000	8000	9000	10000	11000	12000	13000

Figure 5.16: Percent error of efficiency considering second mechanical losses trend.

The error values at low torque and high speed working points confirm what it was noted before, but having an error higher than 2%, another iteration has been done, this time increasing mechanical losses.

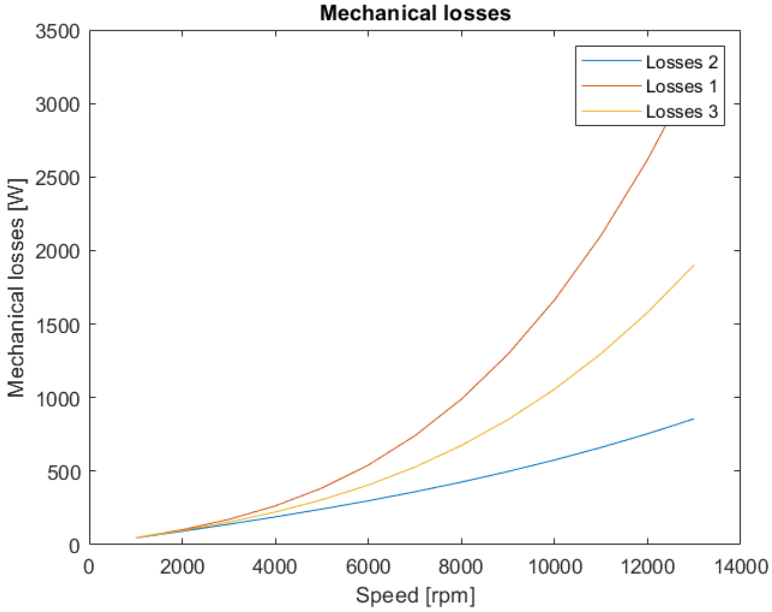

Figure 5.17: Third Mechanical losses trend that has been considered.

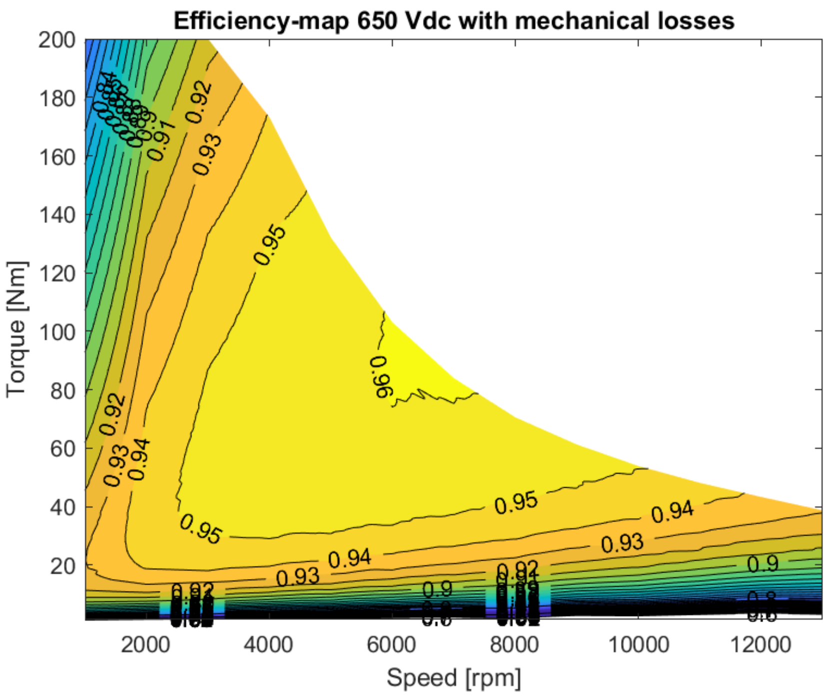

Figure 5.18: Efficiency map considering the third trend of mechanical losses.

Fig.5.18 shows that the last mechanical losses curve decreases the efficiency in the central zone of the map. The second estimation has been considered as correct trend of mechanical losses.

Efficiency on the T-ω plane with third mechanical losses

200	0,7984	0,8839											
180	0,8177	0,8954	0,9240										
160	0,8365	0,9063	0,9315										
140	0,8541	0,9160	0,9379	0,9486									
120	0,8696	0,9243	0,9432	0,9522									
100	0,8842	0,9316	0,9475	0,9548	0,9585								
80	0,8976	0,9380	0,9510	0,9567	0,9593	0,9604							
60	0,9106	0,9433	0,9533	0,9572	0,9586	0,9589	0,9582						
40	0,9225	0,9466	0,9530	0,9547	0,9545	0,9537	0,9517	0,9493	0,9469	0,9438			
20	0,9298	0,9425	0,9439	0,9424	0,9394	0,9355	0,9310	0,9260	0,9205	0,9146	0,9083	0,9017	0,8947
	1000	2000	3000	4000	5000	6000	7000	8000	9000	10000	11000	12000	13000

Figure 5.19: Efficiency values considering third trend of mechanical losses.

Efficiency percent error with third mechanical losses

200	12,32	7,23											
180	8,28	5,63	2,06										
160	4,36	3,45	1,77										
140	3,99	1,75	1,38	1,43									
120	3,40	1,33	0,87	1,18									
100	2,17	1,14	0,58	0,50	0,89								
80	1,52	0,80	0,10	0,07	0,07	0,56							
60	1,17	0,88	0,34	0,02	0,15	0,12	0,33						
40	1,35	1,22	0,84	0,28	0,58	0,66	0,34	0,29	0,20	0,40			
20	2,67	2,38	2,53	1,31	0,06	0,59	0,96	0,43	1,03	2,23	2,39	2,03	0,59
	1000	2000	3000	4000	5000	6000	7000	8000	9000	10000	11000	12000	13000

Figure 5.20: Percent error of efficiency considering third mechanical losses trend.

Once low torque behaviour has been analysed, mechanical losses are considered, but all maps share some points with high error. In detail, all points with high torque value have an error higher than 10%, that is not acceptable. This could be linked to the conditions in which efficiency maps in [2] are extracted.
Nominal torque of the machine is 140 Nm, with a current supply of 120 Amps. All points over this value of torque work in different conditions, overload conditions. In overload condition, the motor could work at higher temperature. Being a permanent magnet motor the temperature has a great influence on the behaviour of the machine. As shown in Chapter 1 and Chapter 2, magnets, so the flux in the machine, are really temperature-sensitive. For this reason each point over 140 Nm of torque has to be analyzed in other conditions. To prove this claim, all tests described so far were repeated at a temperature of 150 °C, that can be a valid value since the tests described in [2] indicate a temperature reached in overload conditions equal to this. Once obtained all inputs described in this work thesis, the efficiency was calculated only for interested point, over the torque value of 140 Nm.

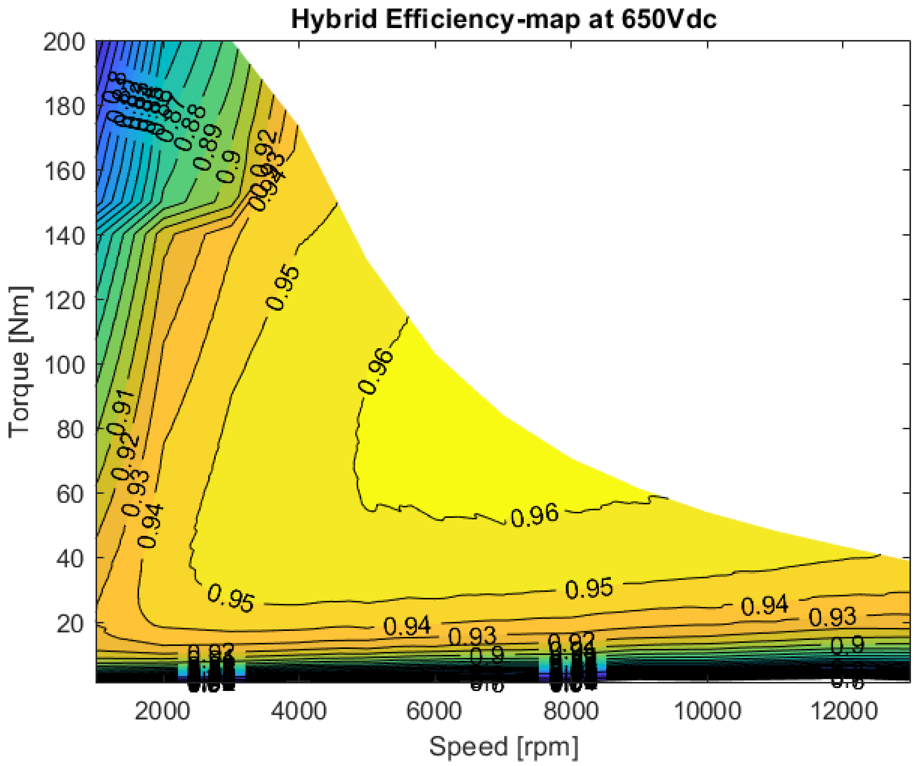

Figure 5.21: Efficiency map considering the second trend of mechanical losses and overloading conditions.

Efficiency on the T-ω plane hybrid method

200	0,7599	0,8511											
180	0,7828	0,8646	0,8934										
160	0,8028	0,8763	0,9012										
140	0,8230	0,8880	0,9099	0,9492									
120	0,8696	0,9245	0,9435	0,9528									
100	0,8843	0,9318	0,9479	0,9555	0,9596								
80	0,8977	0,9382	0,9515	0,9576	0,9607	0,9624							
60	0,9107	0,9437	0,9540	0,9584	0,9604	0,9615	0,9617						
40	0,9226	0,9470	0,9540	0,9565	0,9572	0,9575	0,9569	0,9559	0,9552	0,9539			
20	0,9301	0,9434	0,9459	0,9458	0,9446	0,9429	0,9408	0,9386	0,9362	0,9337	0,9312	0,9285	0,9258
	1000	2000	3000	4000	5000	6000	7000	8000	9000	10000	11000	12000	13000

Figure 5.22: Efficiency values of the hybrid map.

Efficiency percent error hybrid method

200	7,89	3,65											
180	4,19	2,26	1,30										
160	0,35	0,14	1,53										
140	0,37	1,36	1,66	1,50									
120	3,40	1,35	0,90	1,24									
100	2,18	1,16	0,62	0,57	1,01								
80	1,52	0,82	0,16	0,16	0,07	0,77							
60	1,18	0,92	0,42	0,14	0,04	0,15	0,69						
40	1,37	1,27	0,94	0,47	0,30	0,26	0,19	0,41	1,07	1,46			
20	2,69	2,48	2,73	1,67	0,49	1,37	0,09	0,92	0,66	0,14	0,12	0,91	2,78
	1000	2000	3000	4000	5000	6000	7000	8000	9000	10000	11000	12000	13000

Figure 5.23: Percent error of efficiency considering hybrid map.

As shown in fig.5.21 and in fig.5.23, at the overload points there is a clear improvement in the calculated efficiency (the error has been almost halved). Some points continue to have a high value of error, but it is normal because refer values have been obtained by experimental tests, so being overload conditions other factors could increase losses (i.e. saturation,...).

5.2.1 Efficiency map at a different voltage value

Not having reference results for analysis at different voltages, only one study has been provided. A value of 400 Vdc has been chosen in order to explain what happened. Changing the voltage supply, the only charachyeristic of the machine that changes is the base-speed: if the voltage increases, the base-speed increases too, otherwise if the voltage decreases, the base-speed decreases too. As shown in fig.5.24 a test at a lower voltage would have reduced the base speed too much. 400 V is a fair compromise to show the differences.

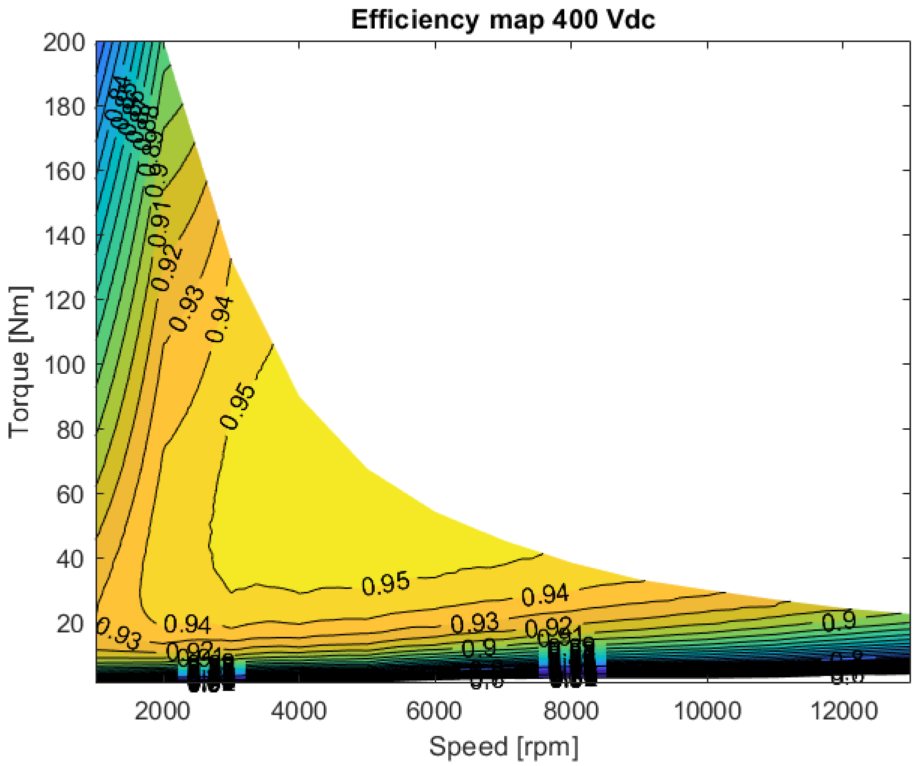

Figure 5.24: Efficiency map at 400 Vdc.

Conclusions

The direction taken by the automotive industry of vehicle electrification has led to the development of methods for analysing and studying hybrid and electric power-trains is needed.
The aim of this thesis work was to evaluate a new way of describing the behaviour of an electric machine under different operating conditions (e.g. at different supply voltages). As mentioned in the introduction, the target of this method is to describe the electric motor by means of efficiency maps, thanks to which it would be possible to make a prediction of the thermal behaviour of the system.

Since we do not have the actual values of the mechanical losses of the analyzed machine, and actually it is a first approach to the technique, the losses values adopted belong to the literature. Using them, it was possible to analyse if the approach works.

The theoretical results obtained show good accuracy of the strategy at normal working points and a different behaviour in overload conditions. Under the latter conditions, temperature becomes a critical parameter for permanent magnet motors, such as the one analysed in this work. Several simulations at different temperature values are needed due to the demagnetization of the magnets, but this is caused by the type of the machine, not by the method.
A strength of this method is the reduced computation time needed, once all the parameters of the algebraic model are available, to obtain the efficiency maps with different maximum voltage and current values.
Even though the theory studied and exposed in Chapter 4 eliges the second method as the one to be adopted, another possible future step might be the analysis of the machine exploiting the first one to numerical state the one which better fits the problem.
Furthermore, a thermal study of the machine could be carried out to compare the real behaviour of the machine with that simulated from the data obtained in this thesis work.

Appendix A

Flux maps

A.1 Python code used in Altair Flux.

```
    I_D=[-200,-180,-160,-140,-120,-100,-80,-60,-40,-20,0,
    20,40,60,80,100,120,140,160,180,200];
I_Q=0;

#inizializzo tutte le stringhe che mi serviranno
numero=0;
prefisso1='LAMBDA_1_';
prefisso2='LAMBDA_2_';
prefisso3='LAMBDA_3_';
curvaestrattaa='CURVA_ESTRATTA_A_';
curvaestrattab='CURVA_ESTRATTA_B_';
curvaestrattac='CURVA_ESTRATTA_C_';
fft1='FFT_1_';
fft2='FFT_2_';
fft3='FFT_3_';

#inizio il ciclo sui diversi valori di Id

for d in range(0,21,1):
  numero+=1;
  n=str(numero);

  #creazione grafici flusso fase 1

  flusso1=prefisso1+n;
  curva1=curvaestrattaa+n;
  flux1=fft1+n;

  EvolutiveCurve2D(name=flusso1,
```

```
                evolutivePath=EvolutivePath(parameterSet=[
SetParameterFixed(paramEvol=VariationParameter['I_D'],

            currentValue=I_D[d]),

SetParameterXVariable(paramEvol=VariationParameter['
ANGPOS_ROTOR'],

                limitMin=1.0,

                limitMax=91.0)]),
                formula=['LAMBDA_1'])

#creazione fft di flusso1

result = SpectrumAnalysis(curve=Curve2d[flusso1],
                component='LAMBDA_1',
                cycle=FullCycle(),
                numberHarmonics=10,
                computeDCComponent=NonContinue(),
                scaleDecibel=FirstHarmonic(firstHarmonicValue
=100.0),
                nameRebuiltCurve=curva1,
                nameFourierTransform=flux1)

#creazione grafici flusso fase 2

flusso2=prefisso2+n;
curva2=curvaestrattab+n;
flux2=fft2+n;

EvolutiveCurve2D(name=flusso2,
        evolutivePath=EvolutivePath(parameterSet=[
SetParameterFixed(paramEvol=VariationParameter['I_D'],

    currentValue=I_D[d]),

SetParameterXVariable(paramEvol=VariationParameter['
ANGPOS_ROTOR'],

        limitMin=1.0,

        limitMax=91.0)]),
         formula=['LAMBDA_2'])

#creazione fft flusso 2

result = SpectrumAnalysis(curve=Curve2d[flusso2],
                component='LAMBDA_2',
```

```
                    cycle=FullCycle(),
                    numberHarmonics=10,
                    computeDCComponent=NonContinue(),
                    scaleDecibel=FirstHarmonic(firstHarmonicValue
 =100.0),
                    nameRebuiltCurve=curva2,
                    nameFourierTransform=flux2)

#creazione grafici flusso fase 3

flusso3=prefisso3+n;
curva3=curvaestrattac+n;
flux3=fft3+n;

EvolutiveCurve2D(name=flusso3,
              evolutivePath=EvolutivePath(parameterSet=[
 SetParameterFixed(paramEvol=VariationParameter['I_D'],

          currentValue=I_D[d]),

 SetParameterXVariable(paramEvol=VariationParameter['
 ANGPOS_ROTOR'],

               limitMin=1.0,

               limitMax=91.0)]),
               formula=['LAMBDA_3'])



result = SpectrumAnalysis(curve=Curve2d[flusso3],
                    component='LAMBDA_3',
                    cycle=FullCycle(),
                    numberHarmonics=10,
                    computeDCComponent=NonContinue(),
                    scaleDecibel=FirstHarmonic(firstHarmonicValue
 =100.0),
                    nameRebuiltCurve=curva3,
                    nameFourierTransform=flux3)

#estrazione grafici flusso fase 1

CurveVariation2D[flux1].exportExcel(xlsFile='fft_flusso1_iq0',
             mode='add')

#estrazione grafici flusso fase 2

CurveVariation2D[flux2].exportExcel(xlsFile='fft_flusso2_iq0',
             mode='add')
```

```

#estrazione grafici flusso fase 3

CurveVariation2D[flux3].exportExcel(xlsFile='fft_flusso3_iq0',
          mode='add')
```

A.2 MATLAB code used to compute Flux Maps.

```
f1='FFT_1_';
f2='FFT_2_';
f3='FFT_3_';
k_1='LAMBDA_1_';
k_2='LAMBDA_2_';
k_3='LAMBDA_3_';
speed=1000; %rpm
omega=2*pi*speed/60*8/2;  %rad/sec
phi=74+90;     %gradi

%creo la variabile tempo da inserire nella matrice di rotazione
t=0;
deltat=(2*pi)/omega/90;

%i=0;

%inizializzo matrici di flusso
lambda1=zeros(91,21);
lambda2=zeros(91,21);
lambda3=zeros(91,21);

lambda_alfa=zeros(91,21);
lambda_beta=zeros(91,21);

lambda_d_iq0=zeros(91,21);
lambda_q_iq0=zeros(91,21);

flusso_d_fondamentale_iq0=zeros(1,21);
flusso_q_fondamentale_iq0=zeros(1,21);

lambda_123=zeros(3,1);
lambda_alfabeta=zeros(2,1);

lambda_dq=zeros(2,1);

%inizializzo il valore di fondamentale e la fase iniziale
lambda_max_1=0;
```

```
lambda_max_2=0;
lambda_max_3=0;
phase_1=0;
phase_2=0;
phase_3=0;

%matrice trasformazione trifase-bifase

T=[2/3 -1/3 -1/3;0 sqrt(3)/3 -sqrt(3)/3];

%matrice di rotazione

%R=[cos(omega*t+deltat-4*phi*pi/180) sin(omega*t-4*phi*pi/180); -
    sin(omega*t-4*phi*pi/180) cos(omega*t-4*phi*pi/180)];

%inizializzo numero che servirà per conoscere la posizione in cui
    estrarre
%il valore di flusso
n=0;
numero=0;

%estrazione dei dati
for i=1:21
     n=n+1;
     numero = num2str(n);
     %creo stringhe per riconoscere il foglio  excel
     flusso1=strcat(f1,numero);
     flusso2=strcat(f2,numero);
     flusso3=strcat(f3,numero);
     k1=strcat(k_1,numero);
     k2=strcat(k_2,numero);
     k3=strcat(k_3,numero);

     %estraggo i valori di flusso di fonadamentale e fase iniziale
    flusso 1
     lambda_max_1=cell2mat(readcell('fft_flusso1_iq0.xls','Sheet',
    flusso1,'Range','C20:C20'));
     phase_1=cell2mat(readcell('fft_flusso1_iq0.xls','Sheet',
    flusso1,'Range','E20:E20'));
     l1(:,i)=cell2mat(readcell('flusso1_iq0.xls','Sheet',k1,'Range'
    ,'C16:C106'));


     %estraggo i valori di flusso di fondamentale e fase iniziale
    flusso 2
     lambda_max_2=cell2mat(readcell('fft_flusso2_iq0.xls','Sheet',
    flusso2,'Range','C20:C20'));
     phase_2=cell2mat(readcell('fft_flusso2_iq0.xls','Sheet',
    flusso2,'Range','E20:E20'));
```

```
    l2(:,i)=cell2mat(readcell('flusso2_iq0.xls','Sheet',k2,'Range'
   ,'C16:C106'));

    %estraggo i valori di flusso di fondamentale e fase iniziale
   flusso 3
    lambda_max_3=cell2mat(readcell('fft_flusso3_iq0.xls','Sheet',
   flusso3,'Range','C20:C20'));
    phase_3=cell2mat(readcell('fft_flusso3_iq0.xls','Sheet',
   flusso3,'Range','E20:E20'));
    l3(:,i)=cell2mat(readcell('flusso3_iq0.xls','Sheet',k3,'Range'
   ,'C16:C106'));

    %creazione delle curve di fondamentale
    %t=deltat;

    for c=1:91
        lambda1(c,i)=lambda_max_1*cos(4*c*pi/180+phase_1);
        lambda2(c,i)=lambda_max_2*cos(4*c*pi/180+phase_2);
        lambda3(c,i)=lambda_max_3*cos(4*c*pi/180+phase_3);
    end

    t=deltat;
    for s=1:91
        lambda_123(1,1)=lambda1(s,i);
        lambda_123(2,1)=lambda2(s,i);
        lambda_123(3,1)=lambda3(s,i);

        lambda_alfabeta=T*lambda_123;
        lambda_alfa(s,i)=lambda_alfabeta(1,1);
        lambda_beta(s,i)=lambda_alfabeta(2,1);

        R=[cos(omega*t-4*phi*pi/180) sin(omega*t-4*phi*pi/180); -
   sin(omega*t-4*phi*pi/180) cos(omega*t-4*phi*pi/180)];

        lambda_dq=R*lambda_alfabeta;

        lambda_d_iq0(s,i)=lambda_dq(1,1);
        lambda_q_iq0(s,i)=lambda_dq(2,1);
        t=t+deltat;
    end

    flusso_d_fondamentale_iq0(1,i)=mean(lambda_d_iq0(:,i));
    flusso_q_fondamentale_iq0(1,i)=mean(lambda_q_iq0(:,i));

end

    %essendo simulazioni pesanti computazionalmente faccio questo
   processo
```

```
    %per 11 valori di iq diversi (da 0 a 200 A) e alla fine salvo i dati
    %finali in un'unica matrice
```

Appendix B

Equivalent iron resistance map.

B.1 MATLAB code used to extract iron losses and compute equivalent iron resistance.

```
    %anche per il calcolo delle perdite è stata fatta una divisione delle
%simulazioni in base alla velocità però, quindi questo codice sarà adattato
%ad ogni diverso valore di velocità

Perdite_1000=zeros(6,6);
Resistenza_ferro_1000=zeros(6,6);
R_fe_1000=zeros(201,201);
r_tmp=zeros(6,201);
prefisso='PERDITE_';
load("Mappa_flussi_ristretta.mat")
numero=0;
speed=1000;
p=4;
omega=2*pi*speed/60*p;

%prendo i dati estratti da flux e formo due matrici: una di perdite e una di
%resistenza equivalente del ferro

for q=1:6
    for d=1:6
        numero=numero+1;
        n=num2str(numero);
```

```
        stringa=strcat(prefisso,n);
        Perdite_1000(end-(q-1),d)=8*cell2mat(readcell('Perdite.xls
    ','Sheet',stringa,'Range','C107:C107'));
        Resistenza_ferro_1000(end-(q-1),d)=(flusso_q_fondamentale(
    end-(q-1),d)^2+flusso_d_fondamentale(end-(q-1),d)^2)*omega^2/
    Perdite_1000(end-(q-1),d);
    end
end

%interpolo i valori di resistenza in modo da avere delle matrici
    che siano
%delle stesse dimensioni di quelle dei flussi

Id=-200:40:0;
id=-200:1:0;
n=0;
%interpolazione id
for i=1:40:201
    n=n+1;
    q=polyfit(Id,Resistenza_ferro_1000(n,:),5);
    R_fe_1000(i,:) = polyval(q,id);
end

n=0;
for i=1:40:201
    n=n+1;
    r_tmp(n,:)=R_fe_1000(i,:);
end

Iq=200:-40:0;
iq=200:-1:0;
n=0;
%interpolazione iq
for i=1:201
    n=n+1;
    q=polyfit(Iq,r_tmp(:,n),5);
    R_fe_1000(:,i) = polyval(q,iq);
end

n=0;
for i=1:40:201
    n=n+1;
    figure(i)
    plot(Id,Resistenza_ferro_1000(n,:))
    hold on
    plot(id,R_fe_1000(i,:))
end
```

B.2 MATLAB code used to compute equivalent iron resistance map.

```
% vado a trovare la rfe al variare della velocità in tutto il
    piano T-w,
% anche sopra l'MTPS, prendendo in considerazione le condizioni di
     minime perdite

load("flussi_interpolati")
load("Perdite_ferro_fitte.mat")
load("Resistenza_ferro_mappate_velocità_fitte.mat")
coppia=zeros(201,201);
T_analysed=0:1:200;
p=4;
id=-200:1:0;
iq=200:-1:0;
perdite_minime=50000;
R_21=0.077;
Temperature=120;
R=R_21*(235+Temperature)/(235+21);
perdite_totali=zeros(201,13);
torque=zeros(201,13);
ptot=0;
pfe=zeros(201,13);
rfe=zeros(201,13);
rfe_tmp=zeros(201,201);
index_d=zeros(201,13);
index_q=zeros(201,13);
ppp=[];

%calcolo la coppia in tutti i punti del piano id iq con id
    negative
for d=1:201
     for q=1:201
     coppia(q,d)=12*((flusso_d_interp(q,d)*iq(q))-(flusso_q_interp(
    q,d)*id(d)))/2;
     end
end

%mi trovo tutte le combinazioni di corrente che mi danno i valori
    di coppia
%che voglio analizzare
T_temp=contourc(id,iq',coppia,T_analysed);

%le inserisco tutti in due matrici (id e iq) dove le righe
    indicano i
%valori di coppia
```

```
i=1;
step=1;
index=0;
id_torque=zeros(length(T_analysed),length(T_temp(1,:)));
iq_torque=zeros(length(T_analysed),length(T_temp(1,:)));

while i<=length(T_analysed)
    while T_temp(1,step)==T_analysed(i)
        index=T_temp(2,step);
        id_temp=T_temp(1,step+1:step+index);
        iq_temp=T_temp(2,step+1:step+index);
        id_torque(i,:)=[id_temp nan*ones(1,length(T_temp(1,:))-length(id_temp))];
        iq_torque(i,:)=[iq_temp nan*ones(1,length(T_temp(1,:))-length(iq_temp))];
        if (step+index)<=length(T_temp)
            step=step+index+1;
            i=i+1;
        end
        if step>length(T_temp(1,:))
            break;
        end
    end
end

%arrotondo perchè la funzione contourc interpola e prende valori di
%corrente che non hanno una corrispondenza di flusso nelle matrici di
%flusso estratte da flux
 id_t=round(id_torque);
 iq_t=round(iq_torque);

 %analisi a diverse velocità e diversi valori di coppia del punto con
 %minime perdite. di quel punto salvo indici d e q e rfe

 for v=1:13
     ptot=0;
     perdite_minime=50000;
     if v==1
         p_tmp=Pfe_1000;
         rfe_tmp=R_fe_1000;
     end
     if v==2
         p_tmp=Pfe_2000;
         rfe_tmp=R_fe_2000;
     end
     if v==3
```

```
            p_tmp=Pfe_3000;
            rfe_tmp=R_fe_3000;
        end
        if v==4
            p_tmp=Pfe_4000;
            rfe_tmp=R_fe_4000;
        end
        if v==5
            p_tmp=Pfe_5000;
            rfe_tmp=R_fe_5000;
        end
        if v==6
            p_tmp=Pfe_6000;
            rfe_tmp=R_fe_6000;
        end
        if v==7
            p_tmp=Pfe_7000;
            rfe_tmp=R_fe_7000;
        end
        if v==8
            p_tmp=Pfe_8000;
            rfe_tmp=R_fe_8000;
        end
        if v==9
            p_tmp=Pfe_9000;
            rfe_tmp=R_fe_9000;
        end
        if v==10
            p_tmp=Pfe_10000;
            rfe_tmp=R_fe_10000;
        end
        if v==11
            p_tmp=Pfe_11000;
            rfe_tmp=R_fe_11000;
        end
        if v==12
            p_tmp=Pfe_12000;
            rfe_tmp=R_fe_12000;
        end
        if v==13
            p_tmp=Pfe_13000;
            rfe_tmp=R_fe_13000;
        end

        for c=1:length(T_analysed)
            perdite_minime=50000;
            ptot=0;
            ppp=[];
            for i=1:length(id_t)
```

```
                d=find(id==id_t(c,i));
                q=find(iq==iq_t(c,i));
                if (d>=0 & d<=201 & q>=0 & q<=201)
                    ferro=p_tmp(q,d);
                    rame=3*R*((id(d))^2+(iq(q))^2)/2;
                    ptot=ferro+rame;
                    ppp(i)=ptot;
                    if ptot<perdite_minime
                        perdite_minime=ptot;
                        k=d;
                        j=q;
                        t=3*p*((flusso_d_interp(q,d)*iq(q))-(flusso_q_interp(q,d)*id(d)))/2;
                    end
                end
                pfe(end-(c-1),v)=p_tmp(j,k);
                rfe(end-(c-1),v)=rfe_tmp(j,k);
                index_d(end-(c-1),v)=k;
                index_q(end-(c-1),v)=j;
            end
            min(ppp)
            perdite_totali(end-(c-1),v)=perdite_minime;
            torque(end-(c-1),v)=t;

        end
 end

speed=1000:1000:13000;
T_analysed=200:-1:0;
contourf(speed,T_analysed,rfe,13)
load('MTPS.mat')
velocita=0:1000:13000;
hold on
plot(velocita,MTPS)
```

Appendix C

Efficiency map.

```
%inizializzo i dati, carico tutti i dati estratti nei precedenti
    codici
load("flussi_interpolati.mat")
load("Rfe_T_w_fitta.mat")
load("Perdite_efficiency_map.mat")
load("torque_efficiency_map.mat")
load("indici_dq_perdite_minime.mat")
id=-200:1:0;
iq=200:-1:0;
R_21=0.077;
Temperature=120;
R=R_21*(235+Temperature)/(235+21);
p=4;
omega=2*pi*(1000:1000:13000)/60*p;
speed=zeros(200,13);
meccaniche=zeros(1,13);
perdite_totali=zeros(200,13);

load("MTPS.mat")

x1=MTPS(5):-1:0;

T_analysed=[];
for i=1:200
    speed(i,:)=1000:1000:13000;
end
% for i=1:13
%     T_analysed(:,i)=200:-1:0;
% end

%creo una matrice di coppia analizzata in modo da avere 200 punti
    di coppia
%ad ogni velocità
```

```
T_analysed(:,1)=200:-1:1;
T_analysed(:,2)=200:-1:1;
T_analysed(:,3)=200:-1:1;
T_analysed(:,4)=linspace(MTPS(5),1,200);
T_analysed(:,5)=linspace(MTPS(6),1,200);
T_analysed(:,6)=linspace(MTPS(7),1,200);
T_analysed(:,7)=linspace(MTPS(8),1,200);
T_analysed(:,8)=linspace(MTPS(9),1,200);
T_analysed(:,9)=linspace(MTPS(10),1,200);
T_analysed(:,10)=linspace(MTPS(11),1,200);
T_analysed(:,11)=linspace(MTPS(12),1,200);
T_analysed(:,12)=linspace(MTPS(13),1,200);
T_analysed(:,13)=linspace(MTPS(14),1,200);

efficiency=zeros(201,13);

for s=1:13
    for t=1:201
        %modello circuitale
         Rs_eq=(R*rfe(t,s))/(R+rfe(t,s));
         q=index_q(t,s);
         d=index_d(t,s);
         T=3*p*((flusso_d_interp(q,d)*iq(q)-(flusso_q_interp(q,d)*id(d))))/2;
         is=sqrt(id(d)^2+iq(q)^2);
         Vd_eq=Rs_eq*id(d)-omega(s)*flusso_q_interp(q,d);
         Vq_eq=Rs_eq*iq(q)+omega(s)*flusso_d_interp(q,d);
         Vs_d=((Rs_eq+abs(rfe(t,s)))/abs(rfe(t,s)))*Vd_eq;
         Vs_q=((Rs_eq+abs(rfe(t,s)))/abs(rfe(t,s)))*Vq_eq;
         V=sqrt(Vs_d^2+Vs_q^2);
         Ife_d=-id(d)*Rs_eq/(Rs_eq+rfe(t,s))+Vd_eq/(Rs_eq+rfe(t,s));
         Ife_q=-iq(q)*Rs_eq/(Rs_eq+rfe(t,s))+Vq_eq/(Rs_eq+rfe(t,s));
         ife=sqrt(Ife_d^2+Ife_q^2);
         is_d=id(d)+Ife_d;
         is_q=iq(q)+Ife_q;
         %calcolo tutte le perdite presenti ell'analisi, due casi: uno con perdite per effettto pelle considerate in relazione al prodotto tra corrente e velocità al quadrato, uno non considerando l'effetto pelle
         perdite_totali(t,s)=(3/2)*R*(is_d^2+is_q^2)+(3/2)*rfe(t,s)*ife^2+(1e-6*(omega(s)/p)^3+0.0006*(omega(s)/p)^2+0.43*(omega(s)/p));
%          perdite_totali(t,s)=0.0000005*(is_d^2+is_q^2)*(omega(s)/(p))^2+(3/2)*R*(is_d^2+is_q^2)+(3/2)*rfe(t,s)*ife^2+(1e-6*(omega(s)/p)^3+0.0006*(omega(s)/p)^2+0.43*(omega(s)/p));
         meccaniche(1,s)=(1e-6*(omega(s)/p)^3+0.0006*(omega(s)/p)^2+0.43*(omega(s)/p));
```

```
            efficiency(t,s)=(T*omega(s)/p)/((T*omega(s)/p)+
    perdite_totali(t,s));

     end
end

%creo una nuova matrice che contiene l'interpolazione dell'
    anadamento
%dell'efficienza per ogni velocità in modo da avere 200 punti di
    coppia per
%ogni valore di velocità
eta=zeros(200,13);
eta(:,1)=efficiency(1:end-1,1);
eta(:,2)=efficiency(1:end-1,2);
eta(:,3)=efficiency(1:end-1,3);
eta(:,4)=interp1(MTPS(5):-1:1,efficiency(201-MTPS(5):end-1,4),
    T_analysed(:,4),'spline');
eta(:,5)=interp1(MTPS(6):-1:1,efficiency(201-MTPS(6):end-1,5),
    T_analysed(:,5),'spline');
eta(:,6)=interp1(MTPS(7):-1:1,efficiency(201-MTPS(7):end-1,6),
    T_analysed(:,6),'spline');
eta(:,7)=interp1(MTPS(8):-1:1,efficiency(201-MTPS(8):end-1,7),
    T_analysed(:,7),'spline');
eta(:,8)=interp1(MTPS(9):-1:1,efficiency(201-MTPS(9):end-1,8),
    T_analysed(:,8),'spline');
eta(:,9)=interp1(MTPS(10):-1:1,efficiency(201-MTPS(10):end-1,9),
    T_analysed(:,9),'spline');
eta(:,10)=interp1(MTPS(11):-1:1,efficiency(201-MTPS(11):end-1,10),
    T_analysed(:,10),'spline');
eta(:,11)=interp1(MTPS(12):-1:1,efficiency(201-MTPS(12):end-1,11),
    T_analysed(:,11),'spline');
eta(:,12)=interp1(MTPS(13):-1:1,efficiency(201-MTPS(13):end-1,12),
    T_analysed(:,12),'spline');
eta(:,13)=interp1(MTPS(14):-1:1,efficiency(201-MTPS(14):end-1,13),
    T_analysed(:,13),'spline');

figure(1)
contourf(speed,T_analysed,eta,200,'ShowText','off')
% pcolor
caxis([0.75,0.94])
colormap default

% for i=4:13
%     figure(i)
%     plot(T_analysed(:,i),eta(:,i))
%     hold on
%     plot([200:-1:0],efficiency(:,i))
% end
```

```

figure(2)
plot(speed,meccaniche)
```

Bibliography

[1] Maria Hernandez, Maarten Messagie, Omar Hegazy, Luca Marengo, Oliver Winter, and Joeri Van Mierlo. «Environmental impact of traction electric motors for electric vehicles applications». In: *The International Journal of Life Cycle Assessment* 22 (Jan. 2017). DOI: 10.1007/s11367-015-0973-9 (cit. on p. 5).

[2] Timothy A Burress, Steven L Campbell, Chester Coomer, Curtis William Ayers, Andrew A Wereszczak, Joseph Philip Cunningham, Laura D Marlino, Larry Eugene Seiber, and Hua-Tay Lin. «Evaluation of the 2010 Toyota Prius Hybrid Synergy Drive System». In: (Mar. 2011). DOI: 10.2172/1007833. URL: https://www.osti.gov/biblio/1007833 (cit. on pp. 6, 19, 20, 22, 23, 40, 66, 74).

[3] Gianmario Pellegrino, Alfredo Vagati, Barbara Boazzo, and Paolo Guglielmi. «Comparison of Induction and PM Synchronous Motor Drives for EV Application Including Design Examples». In: *IEEE Transactions on Industry Applications* 48.6 (2012), pp. 2322–2332. DOI: 10.1109/TIA.2012.2227092 (cit. on pp. 9, 10, 13, 14, 17, 18).

[4] Jere Kolehmainen and Jouni Ikaheimo. «Motors With Buried Magnets for Medium-Speed Applications». In: *Energy Conversion, IEEE Transactions on* 23 (Apr. 2008), pp. 86–91. DOI: 10.1109/TEC.2007.914331 (cit. on p. 16).

[5] Michele Bonfante. *Electric vehicle synchronous motors comparison and design.* 2017-2018 (cit. on p. 20).

[6] Giorgio Pietrini. «A systematic approach to the analysis and design of electrical machines for automotive traction applications». PhD thesis. Università di Parma, 2017 (cit. on pp. 20, 38, 44).

[7] Y. Guan, Z. Q. Zhu, I. A. A Afinowi, J. C. Mipo, and P. Farah. «Comparison between induction machine and interior permanent magnet machine for electric vehicle application». In: (2014), pp. 144–150. DOI: 10.1109/ICEMS.2014.7013454 (cit. on p. 20).

[8] Alireza Fatemi. «Design Optimization of Permanent Magnet Machines Over a Target Operating Cycle Using Computationally Efficient Techniques». PhD thesis. Marquette University, 2016 (cit. on p. 20).

[9] Simone Ferrari. *Valutazione sperimentale delle perdite nel ferro e controllo di massima efficienza per motori SyR*. 2020 (cit. on p. 33).

[10] I. Lar and M. M. Radulescu. «Equivalent core-loss resistance identification for interior permanent-magnet synchronous machines». In: (2012), pp. 1667–1671. DOI: 10.1109/ICElMach.2012.6350104 (cit. on p. 33).

[11] Shensheng Wang, Ziqiang Zhu, Adam Pride, Juntao Shi, Rajesh Deodhar, and Chiaki Umemura. «Comparison of Different Winding Configurations for Dual Three-Phase Interior PM Machines in Electric Vehicles». In: *World Electric Vehicle Journal* 13 (Mar. 2022), p. 51. DOI: 10.3390/wevj13030051 (cit. on pp. 38, 42, 44).